SEISMIC INVESTIGATIONS AT THE VATTENFALL EXPERIMENTAL DAM, ÄLVKARLEBY, SWEDEN
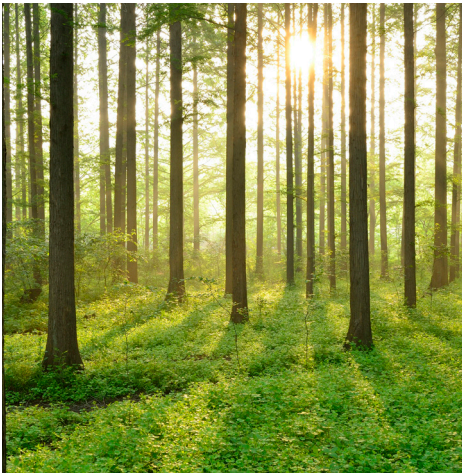
SVENSKT VATTENKRAFTCENTRUM

Energiforsk

SEISMIC INVESTIGATIONS AT THE VATTENFALL EXPERIMENTAL DAM, ÄLVKARLEBY, SWEDEN

November 2019 to December 2020

SILVIA SALAS ROMERO
CHRISTOPHER JUHLIN
EMIL LUNDBERG

Foreword

This project is one of many in the Swedish Hydropower Centre, which aims to improve dam and hydropower safety. A novel method for detecting flaws in dams is evaluated, and some conclusions are drawn on how this method can be developed in the future.

The project was through the Swedish Hydropower Centre, which is a Centre of Excellence funded by the Swedish Energy Agency, Svenska kraftnät, five Swedish universities and the Swedish hydropower industry.

These are the results and conclusions of a project, which is part of a research programme run by Energiforsk. The author/authors are responsible for the content.

Energiforsk

Summary

This report provides an overview of work performed in conjunction with the seismic component for detecting defects in the Vattenfall experimental dam at Älvkarleby through to December 2020. Based on an earlier modelling study it was hypothesized that seismic methods have the potential to detect some flaws in the dam if high enough frequencies can be generated. Dominant frequencies of at least 1500 Hz were considered necessary. The experimental dam was equipped with five seismic cables inside the dam, each containing 24 hydrophones spaced at 0.8 m, giving a total 120 hydrophone pressure sensors. An array of 25 source boreholes, about 0.5-0.6 m deep along the crest, were also built into the dam for allowing borehole sources to generate seismic waves. In addition, four deeper boreholes, extending to the base of the dam, were built into the structure to provide better geometries for measurement of the seismic velocities of the dam materials. A P-wave sparker source was mainly used in the boreholes, but S-wave sources were also tested. Later it was also decided to install a cable on the upstream side of the dam to allow the sparker source to be activated in the water in the reservoir.

Data were acquired in 6 campaigns during the period November 2019 to December 2020 with varying effort during each campaign. Processing of the seismic data to image the defects proved to be a challenge. After much testing a processing routine was established that enabled the characteristic diffraction patterns from small objects to be identified. These are observed on 5 sections, but there is a lack of consistency between recording campaigns. Furthermore, locating the source of the diffractions in space is difficult due to the varying velocity of the different materials (water, filters and core). Complicating the processing are refracted waves along the concrete base and reflections off the sides of the dam, as well as internal reflections from the interfaces between the different materials. It was not possible to clearly identify any defect locations in the dam.

Seismic velocities, both compressional and shear, vary spatially and with time. In the December 2020 measurements, Vp increases from about 450 m/s at the upper levels of the dam to about 1100 m/s near the base, while Vs increases from about 110 m/s to 140 m/s. These velocities are averages over the length of the dam, not values for a given material. They are significantly lower than those expected for a homogeneously saturated core. It is not possible with the current data to determine which path the rays take through the different materials. There is also a trend for increasing Vp velocities with time. In general, Vp increases for each campaign, probably reflecting increasing saturation, and possibly compaction, with time.

A significant conclusion is that sources and sensors should be placed in the saturated zone in order to generate and record the necessary high frequencies required for imaging. Installation of the upstream cable with activation of the sparker in the reservoir allowed frequencies of up to 5000 Hz to be recorded on the sensors at the bottom of the dam that are within the saturated zone. It would have been useful to have installed some permanent geophones for measurement of shear wave velocities. The single three-component sensor used in the experiments was not optimal.

Energiforsk

Keywords:

Sammanfattning

Denna rapport ger en översikt över det arbete som utförts i samband med den seismiska komponenten för att upptäcka defekter i Vattenfalls experimentdammen vid Älvkarleby fram till december 2020. Baserat på en tidigare modellstudie antogs det att seismiska metoder har en potential för att upptäcka vissa defekter i dammar om tillräckligt höga frekvenser kan genereras. Dominanta frekvenser på minst 1500 Hz ansågs nödvändiga. Den experimentella dammen var utrustad med fem seismiska kablar inuti dammen, var och en innehållande 24 hydrofoner med 0,8 m avstånd mellan dem, vilket ger totalt 120 installerade hydrofoner. En uppsättning av 25 källborrhål, cirka 0,5-0,6 m djupa längs krönet byggdes också in i dammen för att generera seismiska vågor. Dessutom byggdes fyra djupare borrhål in i dammen för att ge bättre geometrier för mätning av dammmaterialens seismiska hastigheter. En gnistkälla (sparker) för att generera P-vågor användes främst i borrhålen, men även S-vågskällor testades. Senare beslutades också att installera en kabel på uppströmssidan av dammen för att möjliggöra att gnistkällan aktiveras i vattnet i reservoaren.

Data samlades in i 6 kampanjer under tidsperioden november 2019 till december 2020 med varierande omfattning under varje kampanj. Bearbetning av seismiska data för att avbilda defekterna visade sig vara en utmaning. Efter mycket testning etablerades en bearbetningsrutin som gjorde det möjligt att identifiera de karakteristiska diffraktionsmönstren från små objekt. Dessa observeras på 5 sektioner, men det finns en brist på konsekvens mellan inspelningskampanjerna. Dessutom är det svårt att lokalisera källan till diffraktionerna inom dammen på grund av de olika materialens varierande hastighet (vatten, filter och kärna). Försvårande bearbetningen är brytande vågor längs betongbasen och reflektioner från dammens sidor, samt inre reflektioner från gränssnitten mellan de olika materialen. Det var inte möjligt att definitivt identifiera några skador i dammen.

Seismiska hastigheter, både kompressions- och skjuvningshastigheter, varierar spatialt och med tiden. I december mätningarna ökar Vp från ca 450 m/s på dammens övre nivåer till ca 1100 m/s nära basen, medan Vs ökar från ca 110 m/s till 140 m/s. Dessa hastigheter är medelvärden över dammens längd, inte värden för ett visst material. De är betydligt lägre än vad som förväntas för en homogent mättad kärna. Det är inte möjligt att med nuvarande data avgöra vilken väg strålarna tar genom de olika materialen. Det finns också en trend med ökande Vp-hastigheterna med tiden. I allmänhet ökar Vp för varje kampanj. Detta tolkas för att återspegla ökande mättnad, och möjligen packning, med tiden.

En betydande slutsats är att källor och sensorer bör vara i den mättade zonen för att generera och registrera de nödvändiga höga frekvenserna som krävs för avbildningen. Installation av uppströmskabeln med aktivering av gnistkällan i reservoaren tillät att frekvenser på upp till 5000 Hz kunde registreras på sensorerna i botten av dammen som finns inom den mättade zonen. Det skulle ha varit fördelaktigt att ha installerat några permanenta geofoner för mätning av S-vågshastigheter. Den enda trekomponentssensorn som användes i experimenten var inte optimal.

List of content

Energiforsk

1   Introduction

1.1   BACKGROUND

Embankment dams are the most common dams worldwide (Deangeli et al. 2009). These structures act as water barriers and are classified as earth fill and rock fill dams depending on the amount of natural materials (soil and rock) used in their construction. There are different classes depending on the position of the core, filter, drainage, transition and facing zones. The purpose of these zones is to avoid the loss of soil particles by water seepage (internal erosion and piping), and decrease pore water pressure and the leakage caused by seepage flow through the embankment (Deangeli et al. 2009).

Embankment dam failures are mostly related to overtopping or seepage, and can have devastating effects on the economy and environment as well as loss of human lives (Deangeli et al. 2009; Sharma and Kumar 2013). Failures occur in a great number of cases during the first filling or within five years of the construction of the dam (Sharma and Kumar 2013).

Deterioration of the body and foundation of these structures may also develop progressively along the years of the 'service life'. For example, in the case of Sweden, 60% of the large embankment dams built before 1997 have suffered deterioration in some degree (Norstedt and Nilsson 1997). Increase in outflows and erosion rate may be related to preferential flow directions created by cavities, channels and fracture zones (Kayode et al. 2018). The difficulty in detecting and mapping these damages can be overcome by combining invasive (borehole data) and non-invasive (geophysical data such as resistivity and temperature) investigation techniques, achieving higher lateral resolution and reducing uncertainties (Woolery 2018).

Some examples (Adamo et al. 2020; Ikard et al. 2014; Kim et al. 2007) of non-invasive, cost-effective indirect geophysical methods for evaluating the conditions within embankment dams are: self-potential (sensitive to seepage flows), electro-magnetics (sensitive to saturation, porosity and temperature), electric resistivity tomography (sensitive to saturation, porosity and fluid content), ground penetrating radar (sensitive to buried man-made objects, groundwater and soil/rock interfaces), reflection seismic (sensitive to sinkholes, bedrock interface), magnetics (buried man-made objects), gravity (cavities), and temperature (paths by establishing hydraulic connections). Thus, the information obtained in geophysical surveys can contribute to preventing failure and assessing the dam's structural integrity.

1.2   GOALS OF THE STUDY

Vattenfall initiated a research project to assess the potential of geophysical methods for detecting a number of purpose-built damages within the core of a dam and to monitor its behavior using geotechnical instrumentation. The project was carried out in an experimental dam built in Älvkarleby (Sweden), with flaws of unknown position and size built-in within its core. Construction of the dam

began in 2019 and filling of the dam started in the beginning of 2020. The project is expected to continue to the end of 2022.

The primary objective of the study that we present here was to detect built-in flaws of unknown position and size within the core of the experimental dam using seismic methods (high-resolution P-wave reflection seismic, seismic interferometry and synthetic and real P-wave traveltime tomography). The type of defects included in the core were e.g. a concrete block or gravel of different sizes simulating cavities and channels (Figure 1).

From a geotechnical perspective, a secondary objective of this work was to estimate P- (Vp) and S-wave velocities (Vs), bulk and shear moduli using crosshole seismic experiments, and monitor their changes with time.
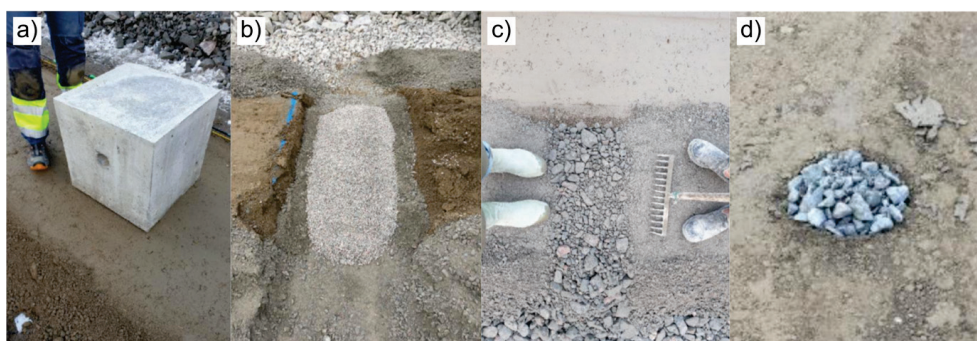

Figure 1. Type of built-in defects: (a) concrete block, (b) elongated shape of fine gravel, (c) elongated shape of coarse gravel, and (d) circular shape of coarse gravel.

1.3 EXAMPLES OF PREVIOUS SEISMIC STUDIES AT OTHER DAMS

As already mentioned, a combination of different methods is more suitable for seepage characterization. Detection of damages using only indirect geophysical methods (e.g. electric resistivity tomography or temperature) is possible, but precise location can be difficult. The use of seismic methods for studying the internal structure and foundation of embankment dams is uncommon. The seismic data are mostly collected in surface seismic surveys on the crest or on the sides of the dam, or near its foundation, and using lower frequency seismic sources than the ones employed in this project.

Shear-wave reflection seismic is a method often used for imaging earth fill dams and their foundations. For example, Woolery (2018) used this method at two dam sites in order to acquire data for detecting low-impedance interfaces and other man-made structures within the dam, and also for estimating depth-to-bedrock.

Refraction seismic, traveltime tomography and surface wave dispersion analysis (e.g. multichannel analysis of surface waves) are the most popular methods for obtaining information about geotechnical properties, depth-to-bedrock, potential paths for seepage flow, fracture zones or degree of saturation in the structure of a dam (Cardarelli et al. 2014; Ivanov 2006 and 2009; Kargaranbafghi and Ghalamzam 2018; Kim et al. 2011; Powers and Burton 2008).

Miller et al. (2004) show a case study using reflection seismic, surface wave analysis and crosshole tomography for investigating a sinkhole at a dam site. Application of these methods proved successful and provided high-resolution data. Low velocity zones, layering within the dam, and subsidence signs were detected combining these seismic methods.

1.4 OUTLINE OF THE REPORT

This report is composed of four main parts summarizing the most important aspects of the seismic research conducted over a 15-month period (Oct 2019 to Dec 2020) at the experimental dam built by Vattenfall in Älvkarleby. The first part describes all the aspects related to data acquisition, such as an overview of the dam geometry, seismic instrumentation installed in the dam, seismic sources and recording campaigns. The second part, data analysis, includes selected results for each methodology (active and passive seismic, P-wave traveltime tomography and seismic interferometry). An analysis of the frequency content of the signals and estimates for Vp and Vs are also presented. The third part, data evaluation, deals with the critical analysis of the potential defects identified in the data, seismic modeling and lessons learned which can be useful for similar research in the future. The final part provides conclusions on the research.

Energiforsk

2 Seismic data acquisition

2.1 OVERVIEW OF DAM GEOMETRY

The construction of the dam and the filling of the water reservoir took around two full months. The dam structure (see Figure 2) is 20 m long, 4 m high and 15 m wide at the bottom and was built within a concrete box (with fiberglass reinforcement at the base). It is composed of four types of material: the central part consists of an impermeable core (A–clay) about 3.5 m high with a thickness of 1.6 m at the bottom and 1.1 m at the top. The core is surrounded by a fine filter (B–sand) 0.5-0.9 m wide on the sides and 0.1 m high on top. On each side of the fine-filter there are two walls of a coarse filter (C–gravel) approximately 0.5 m wide. Covering these materials, support filling (D–crushed stone) is present, extending up to 5.3 m at the bottom in both the upstream and downstream directions with a slope inclination of about 34 degrees.
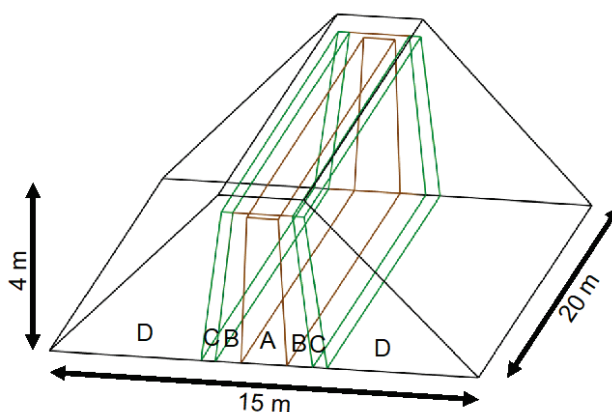

Figure 2. Dam geometry with four types of materials, A–clay (impermeable core), B–sand (fine filter), C–gravel (coarse filter), and D–crushed stone (support filling).

Figure 3. (a) Installation of geophysical equipment (hydrophones (red and black cable) and electrodes (green and black cable)) within the structure of the dam. Boreholes made of PVC casing are approximately 0.55 m deep from the top of the dam. (b) Last works on the crest of the dam before finishing the construction.

In order to comply with the main goals of the general project, geophysical (hydrophones, electrodes and optical fiber for performing seismic, resistivity, temperature and acoustic sensing measurements) and geotechnical (inclinometers, piezometers for doing pore water pressure and strain measurements) equipment were installed within the structure of the dam (Figure 3). Figure 4 and Figure 5 show an overview of the sampling positions for each method. The seismic measurements also required the installation of boreholes (PVC casing) for positioning the borehole sources and a 3C-geophone within the dam. 25 boreholes of approximately 0.5-0.6 m of depth ('shallow') were installed on top of the core (but not extending into the core), along the center of the crest of the dam (named here as BH1001 to BH1025). The borehole spacing was around 0.7 m. To access to deeper levels, four boreholes of 4 m of depth ('deep') were installed at the edges of the dam next to the concrete wall (named as BH6000 to BH9000, two on each side). One of them, BH9000, was not used after the June-July campaign due to the presence of large fractures in the PVC casing.
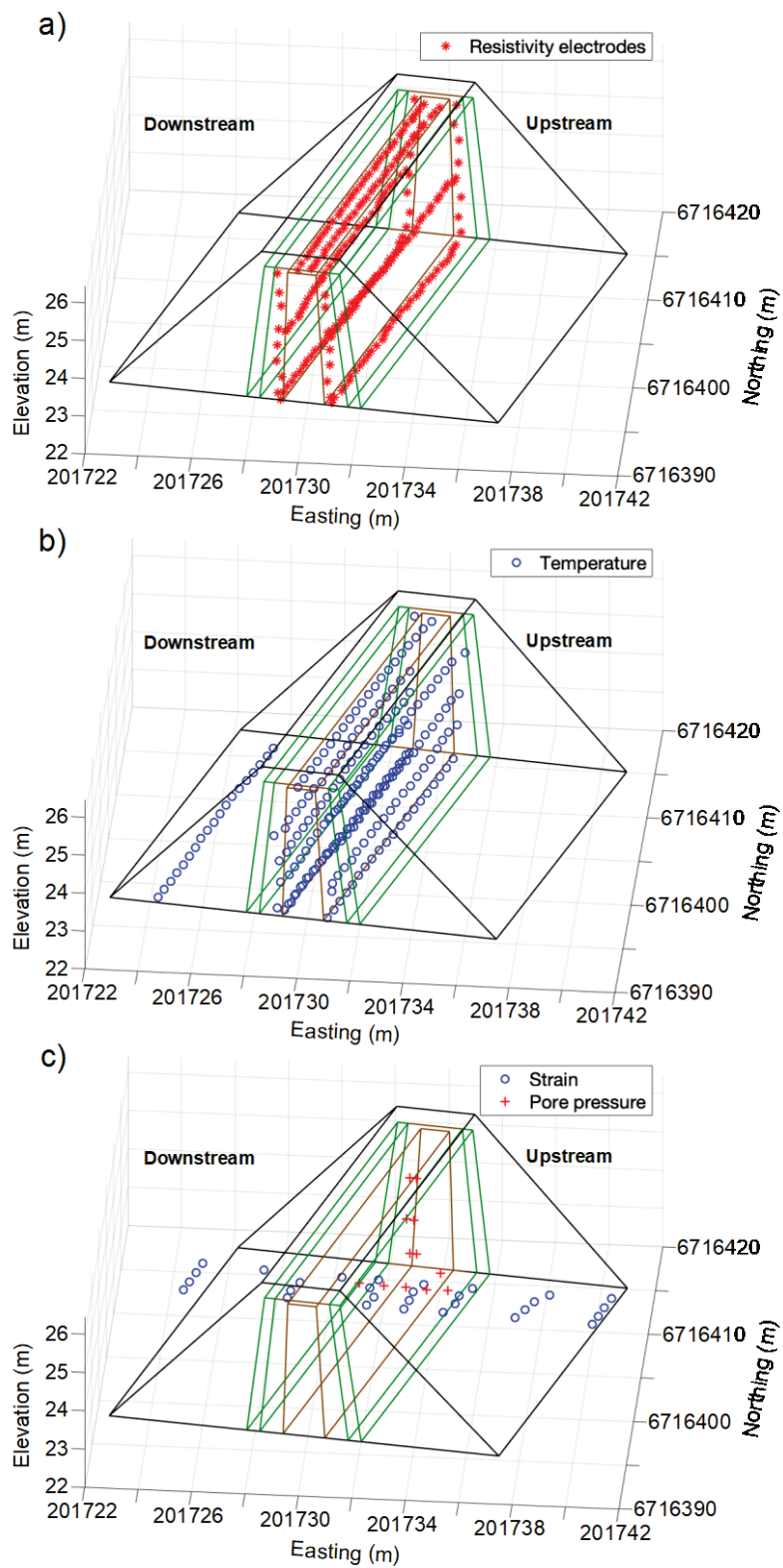
Figure 4. Overview of (a) resistivity, (b) temperature, and (c) strain and pore water pressure sampling point positions.

2.2 INSTRUMENTATION

2.2.1 Hydrophones and hydrophone geometry

The seismic acquisition equipment (see Figure 5) was composed of five lines of 24 hydrophones each. The length of each line was 18.4 m with hydrophones spaced at approximately 0.8 m. Three of the lines were installed on top of the dam's core and two at the bottom on each side of the core, i.e. none of the hydrophone lines were within the core. These lines were named depending on their position within the dam as 1000 (top middle), 2000 (top upstream), 3000 (top downstream), 4000 (bottom upstream), and 5000 (bottom downstream). The lines were powered by battery boxes (AA cells) on the surface, and their strings connected to 24-channel seismographs (Geodes). The hydrophone sensors are characterized as being sensitive to the frequency range 1-10000 Hz.
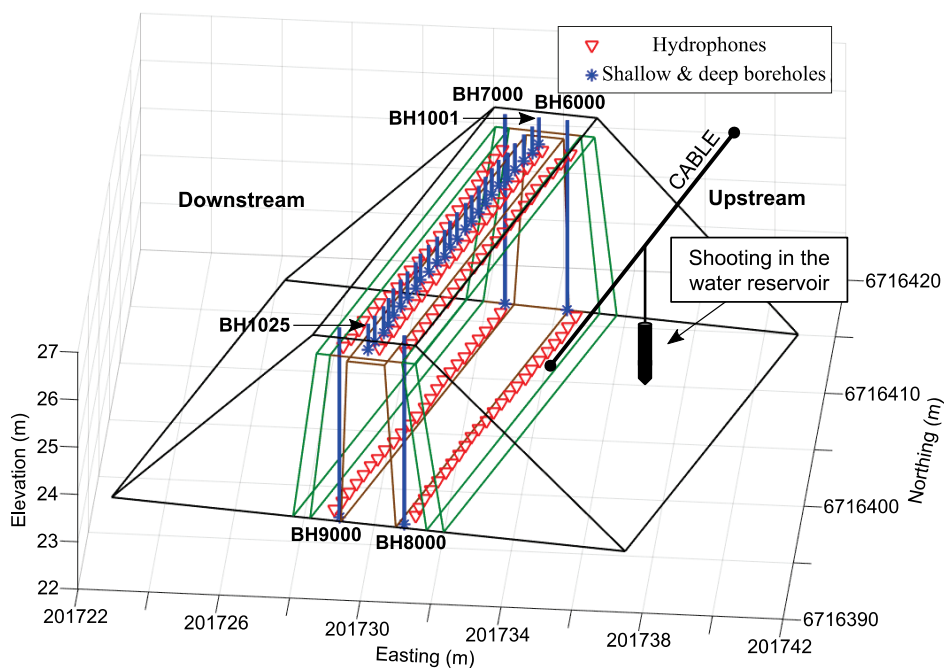

Figure 5. Overview of the installed seismic equipment (hydrophones), and shallow (BH1001 to BH1025) and deep (BH6000 to BH9000) boreholes where seismic sources were used.

2.2.2 BGK3 borehole geophone

The acquisition setup was a combination of all the hydrophone lines and a 3C-borehole geophone (model BGK3, Geotomographie 2021) positioned inside the deep boreholes. The BGK3 borehole geophone is able to record P- and S-waves within dry or water-filled boreholes. In this study all the boreholes were always water filled during data acquisition. The geophone records particle velocity in three directions, vertical and two horizontal components, and its natural frequency is 30 Hz. An inflatable bladder allows to pneumatically couple/clamp the geophone to the borehole wall. A magnetic compass provides the orientation of the

geophone in the borehole with respect to North. During acquisition, the borehole geophone had to be connected to a 24-channel seismograph, with only the first three channels recording. The borehole geophone was positioned at 0.4 m depth intervals, thus nine sampling points were collected per deep borehole.

2.2.3 IPG5000 impulse generator

The IPG5000 impulse generator (Geotomographie 2021) provides high voltage (maximum 5000 V) to the borehole seismic sources, P-wave sparker SBS42 and S-wave source BIS-SH. The energy stored in a large capacitor bank is released through a mechanical switch that can be controlled by a remote-control unit. This unit is connected to one of the Geodes for precise triggering of the signal and allows single or continuous shot release. During data aquisition we used mostly continuous mode as we were shooting about ten times per sampling point for stacking repeated shot records and increasing the signal-to-noise ratio.

2.2.4 P-wave sparker SBS42

The high-frequency borehole seismic source SBS42 (Geotomographie 2021) produces compressional (P) waves in water-filled boreholes. The source, connected to the IPG5000 impulse generator, receives the energy released through a coaxial cable ended by two spark electrodes within a probe. The sparker pulses create vapor bubbles that expand and collapse, generating high-frequency seismic waves. The high-frequency source (up to 5000 Hz) meets the requirements established in a previous 2D/3D seismic modeling study carried out by Uppsala University (Ivandic and Juhlin 2018). This study pointed out the need to use a borehole seismic source able to produce a minimum frequency of 1500 Hz for detecting reasonable sized damages.

In this work, this borehole seismic source was used in the shallow and deep boreholes, as well as in the water reservoir suspended from a cable positioned in the upstream side of the dam as shown in Fig. 5.

2.2.5 S-wave source BIS-SH

BIS-SH borehole seismic source (Geotomographie 2021) produces horizontally polarized shear (SH) and compressional (P) waves in water-filled or dry boreholes (up to 4000 Hz). Energy released by the IPG5000 impulse generator is discharged through a system of coupled coils, which generate a mechanical impact to the borehole wall that generates seismic waves. The hose, oriented perpendicular to the recording direction is connected to a probe that is coupled to the borehole wall by a pneumatic clamping system (inflatable bladder).

The use of this borehole seismic source (only in deep boreholes) was limited due to the failure of the casing in BH9000. The source was not used after the June-July 2020 measurement campaign.

2.2.6 "CHE" CrossHole Energizer

The "CHE" borehole seismic source (PASI 2021) is a hammer able to produce P- and S-waves. The hammer is coupled to the borehole wall by a pneumatic

Energiforsk

clamping system manually controlled by a lever on the surface. Pulling a steel cable joined to the probe-hammer produces a first shot, and then dropping it generates a second shot with inverse (theoretically) polarity.

2.3   RECORDING CAMPAIGNS

Six seismic field campaigns were performed from November 2019 to December 2020 (Figure 6). The seismic data were generally acquired using five Geode-seismographs each recording 24 channels, and connected to a field laptop for collecting the data. The Geodes interconnection allowed recording of a total of 120 channels at the same time. Therefore, all hydrophone lines (120 hydrophones in total) could be recorded simultaneously or a combination of four hydrophone lines with the 3C-borehole geophone. The borehole seismic sources were positioned in the shallow and deep boreholes installed on the crest of the dam (Figure 3). The IPG5000 impulse generator was located inside the container located next to the dam (it had to be protected from water and dust, the same for the connections between the impulse generator and the seismic sources). Control and triggering of the seismic sources were done through the remote-control unit. Additionally, a cable was installed in the upstream side of the dam, above the water reservoir, for hanging the seismic source (Figure 5) and shooting at multiple positions along the cable. Passive data were also collected twice, in campaigns 5 and 6, over several days with recording on 24 (line 4000, October 2020) and 72 channels (lines 2000, 4000 and 5000, November-December 2020).

	November 2019	February 2020	April 2020	June & July 2020	October 2020	November & December 2020
Reservoir saturation	-	-	Partial (reservoir full for 3 weeks)	Partial (reservoir full for 1 month)	Fully saturated	Fully saturated
Water level above bottom part of the dam	-	-	~2.7-3 m	~3.19-3.3 m	~3.17-3.19 m	~3.171 m
Survey parameters						
Receiver type	Hydrophone / 3C-borehole geophone	Hydrophone / 3C-borehole geophone	Hydrophone / 3C-borehole geophone	Hydrophone / 3C-borehole geophone	Hydrophone / 3C-borehole geophone	Hydrophone / 3C-borehole geophone
Recording hydrophone lines / boreholes	1000, 2000, 3000, 4000, & 5000 / BH6000 & BH7000	1000, 2000 & 3000 / BH7000	1000, 2000 & 4000 / BH6000, BH7000 & BH9000	1000, 2000, 3000, 4000, & 5000 / BH6000, BH7000 & BH8000	1000, 2000, 3000, 4000, & 5000 / BH6000, BH7000 & BH8000	1000, 2000, 3000, 4000, & 5000 / BH6000, BH7000 & BH8000
Max. number of active channels	120	72	72	96	120	120
Hydrophone spacing	~ 0.8 m	~ 0.8 m	~ 0.8 m	~ 0.8 m	~ 0.8 m	~ 0.8 m
Borehole geophone sampling within deep boreholes	0.5 m (8 sampling points per borehole)	0.4 m (9 sampling points per borehole)	0.4 m (9 sampling points per borehole)	0.4 m (9 sampling points per borehole)	0.4 m (9 sampling points per borehole)	0.4 m (9 sampling points per borehole)
Source type	SBS42 / CHE	SBS42 / BIS-SH / CHE	SBS42 / BIS-SH	SBS42 / BIS-SH	SBS42	SBS42 / CHE
Shooting boreholes	BH1001-BH1025 / BH8000 & BH9000	BH1001-BH1025 / BH9000	BH1001-BH1025 / BH8000 & BH9000	BH1001-BH1025 / BH6000, BH7000, BH8000 & BH9000	BH1001-BH1025 / BH6000, BH7000 & BH8000	BH1001-BH1025 / BH6000, BH7000 & BH8000
Number of shots	72	70	170	1851	1130	1064
Shot spacing between shallow boreholes and sampling depth	0.8 m / ~0.56 m	0.8 m / ~0.56 m	0.8 m / ~0.56 m	0.8 m / ~0.56 m	0.8 m / ~0.56 m	0.8 m / ~0.56 m
Shot sampling within deep boreholes	1 m (4 sampling points per borehole)	0.8 m (4 sampling points per borehole)	0.8 m (4 sampling points per borehole)	0.8 m (4 sampling points per borehole)	0.8 m (4 sampling points per borehole)	0.8 m (4 sampling points per borehole)
Shot spacing in water reservoir	-	-	-	~0.2 m (100 points)	~0.2 m (100 points)	~0.2 m (100 points)
Recording parameters						
Record length	0.11 s	0.125 s / 0.51 s (borehole)	0.51 s	0.51 s	0.51 s / 0.128 s (water reservoir)/ 4 s (passive)	0.51 s / 0.128 s (water reservoir)/ 4 s (passive)
Sampling rate	0.0625 ms	0.0625 ms / 0.25 ms (borehole)	0.25 ms	0.25 ms	0.25 ms / 0.0625 ms (water reservoir)	0.25 ms / 0.0625 ms (water reservoir) / 2 ms (passive)

Figure 6. Overview of campaigns performed during project period.

Energiforsk

3 Data analysis

3.1 DATA EXAMPLES

Examples of shot gathers for lines 1000 (top middle) and 4000 (bottom upstream) when shooting in the shallow borehole BH1013 (located in the middle of the crest of the dam) and in the middle position along the cable installed above the water reservoir are shown in Figure 7 and Figure 8, respectively.

Figure 7 shows examples of shot gathers when shooting in the shallow borehole for November 2019, June-July and November-December 2020 campaigns. In the case of line 1000 (Figure 7abc), the observed refractions have lower velocity compared to the results from line 4000 (Figure 7def). Line 4000 shows velocities between 400 and 900 m/s. Several reflections are also present in all the gathers of line 4000, showing velocities between 300 and 600 m/s. In Figure 7a (line 1000) a reflection of low velocity is visible.

Energiforsk
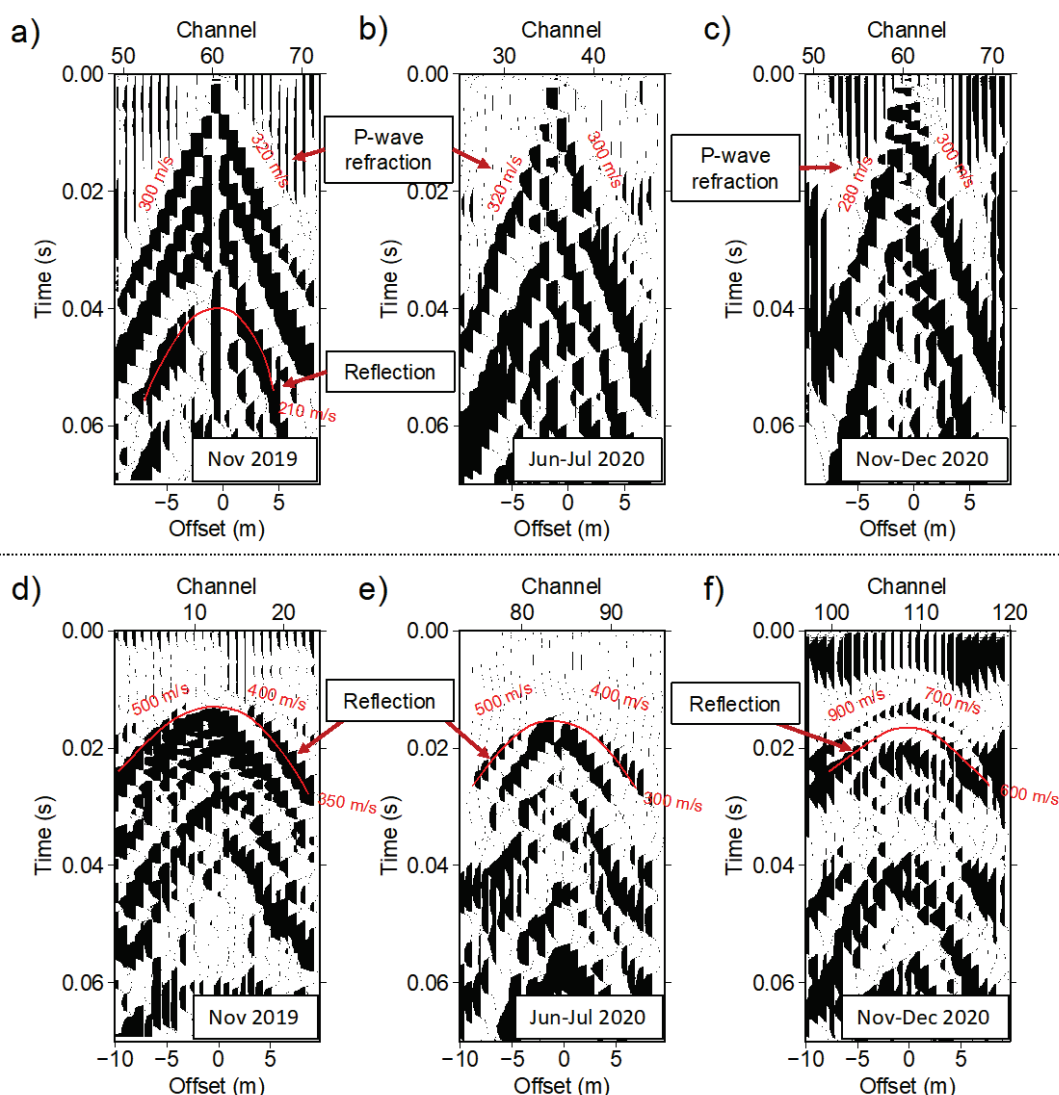
Figure 7. Shot gathers from November 2019, June-July and November-December 2020 campaigns for lines 1000 (a), (b), and (c), and 4000 (d), (e) and (f). Seismic velocities for the different events are also shown. Note that some first arrivals and reflections have velocities close to that of the air wave (330 m/s), suggesting that it is the air wave being identified or that the air wave is interfering with the P-wave.

Figure 8 shows shot gathers when shooting in the water reservoir for the June-July and November-December 2020 campaigns. First arrival velocities (refractions) are higher in line 4000 (Figure 8cd) than in line 1000 (Figure 8ab), ranging between 1600 and 2900 m/s. These velocities are probably due to the path the seismic waves propagate through water and below the concrete basement. In Figure 8a an S-wave refraction is identified, and in Figure 8cd a reflection with a velocity of 1700 m/s. We believe that the 1700 m/s velocity might correspond to the fine filter. The difference in frequency content comparing the arrays and recording campaigns is also evident. Line 4000 has higher frequency content than line 1000, which is also the case between the data collected in June-July and November-December 2020. A faster sampling rate was used in the October and November-December campaigns 2020.
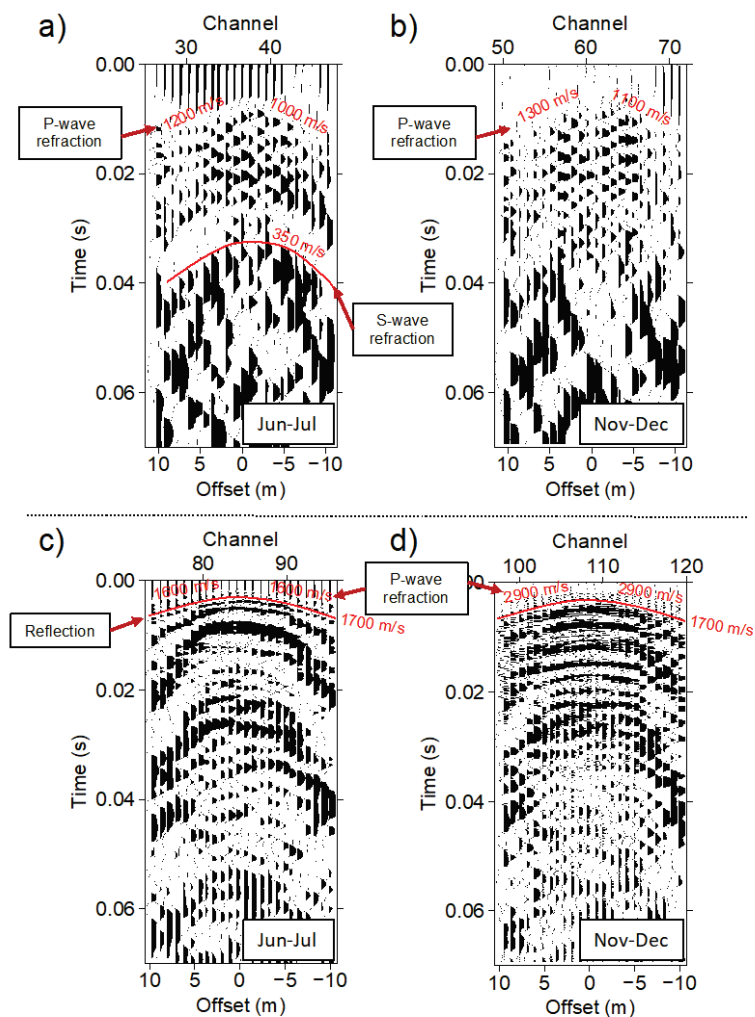
Figure 8. Shot gathers from June -July and November-December campaigns for lines 1000 (a) and (b), and 4000 (c) and (d). Seismic velocities for the different events are also shown.

3.2 FREQUENCY CONTENT OF SIGNALS RECORDED ON THE DIFFERENT HYDROPHONE ARRAYS AND CAMPAIGNS

The analysis of the frequency content is focused on two of the lines, 1000 (top middle) and 4000 (bottom upstream), when shooting in the shallow borehole BH1013 and in the middle position along the cable installed above the water reservoir. The analysis and comparison were done for the same shot ID in each recording campaign (data are separated in 'dam' and 'water reservoir' depending on the shot position), and for the first 20 ms of the recording signal.

In order to reduce the loss of energy when using the P-wave sparker SBS42, plugs of cork, wood, rubber and steel (Figure 9ab) were custom-made to fit the borehole diameter and positioned on top of the probe of the P-wave sparker SBS42 (Figure 9cd). In the October 2020 campaign, plugs of wood, cork and rubber were used, and in the November-December 2020 campaign the steel plug was used. Figure 10 shows the power spectrum diagram for line 1000 when shooting in the dam

(BH1013). All the curves show similar trends and amplitudes. The data collected in the November-December 2020 campaign seem to have slightly higher amplitudes compared to the others. These values may be due to a higher degree of saturation (although the dam was already considered fully saturated in October 2020) or related to the use of the steel plug covering the borehole entry.
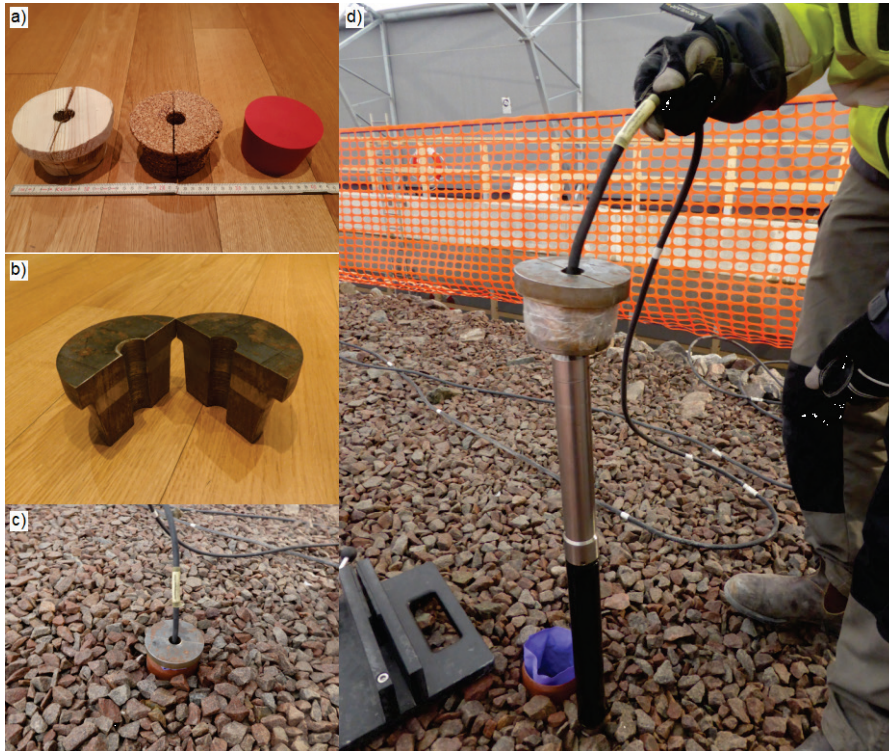

Figure 9. (a) Plugs of wood, cork and rubber used in the shallow boreholes in the October 2020 campaign. (b) Steel plug (made by Vattenfall) used in the November-December 2020 campaign. (c) and (d) Fitting the plug to the top part of the probe of the P-wave spar
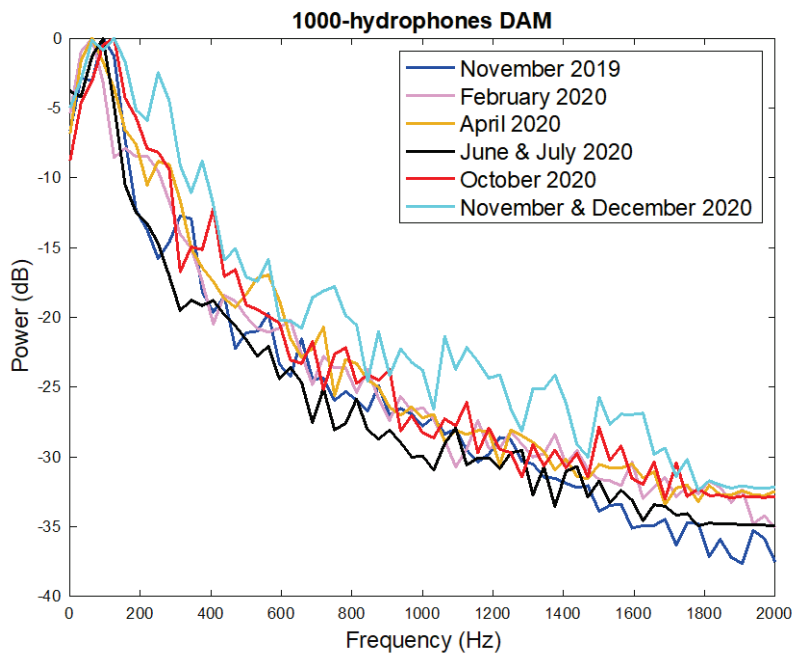
Figure 10. Power spectrum diagram showing the frequency content obtained in line 1000 (top middle) for the different recording campaigns (see color codes in legend). Shot position BH1013.
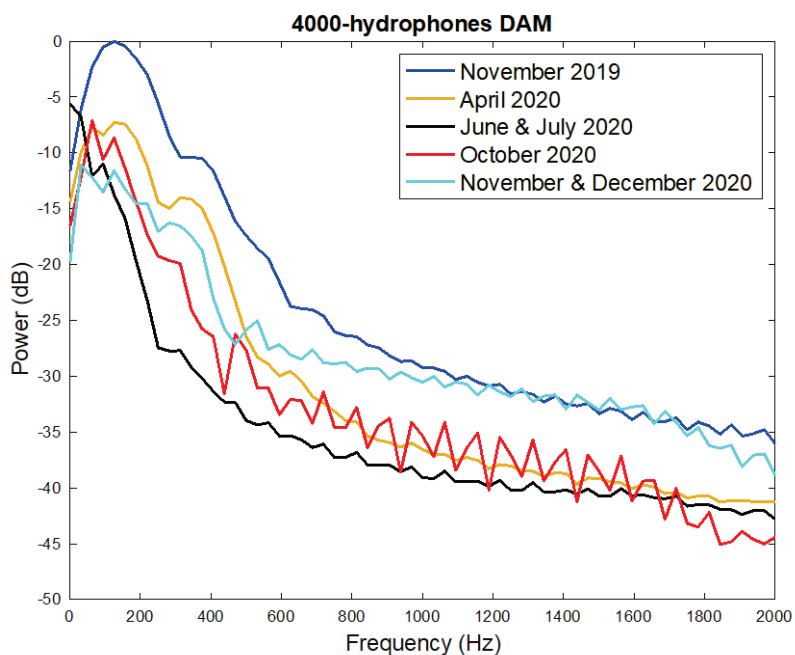

Figure 11. Power spectrum diagram showing the frequency content obtained in line 4000 (bottom upstream) for the recording campaigns where this dataset was collected (see color codes in legend). Shot position BH1013.

In the case of line 4000 (Figure 11) when shooting in the dam (BH1013), the frequency content changes between the different campaigns. Curiously, the highest amplitudes were recorded on November 2019 campaign, when the reservoir was empty. On the November-December 2020 campaign the frequency content is also higher compared to the other datasets.
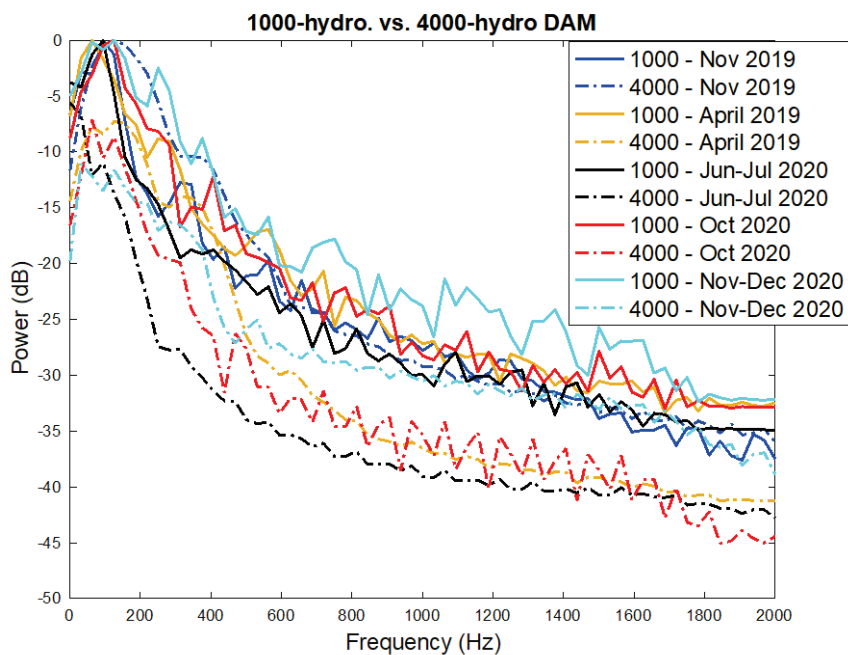
Figure 12. Power spectrum diagram showing the comparison of the frequency content obtained in lines 1000 and 4000. This figure shows the same information shown in Figs. 14 and 15.

Figure 12 shows the data comparison between lines 1000 and 4000. In general, the amplitudes are higher in line 1000 compared to line 4000 for all recording campaigns. Line 4000 only shows higher frequency content in the last recording campaign (Nov-Dec 2020 – cyan line), but still line 1000 has higher amplitudes. These high amplitudes are probably related to background noise and the proximity to the source point in line 1000. Note also that the difference between the lines is small when the reservoir was empty in November 2019, and larger in the rest of the campaigns (the difference seems smaller for the data recorded in the last recording campaign).
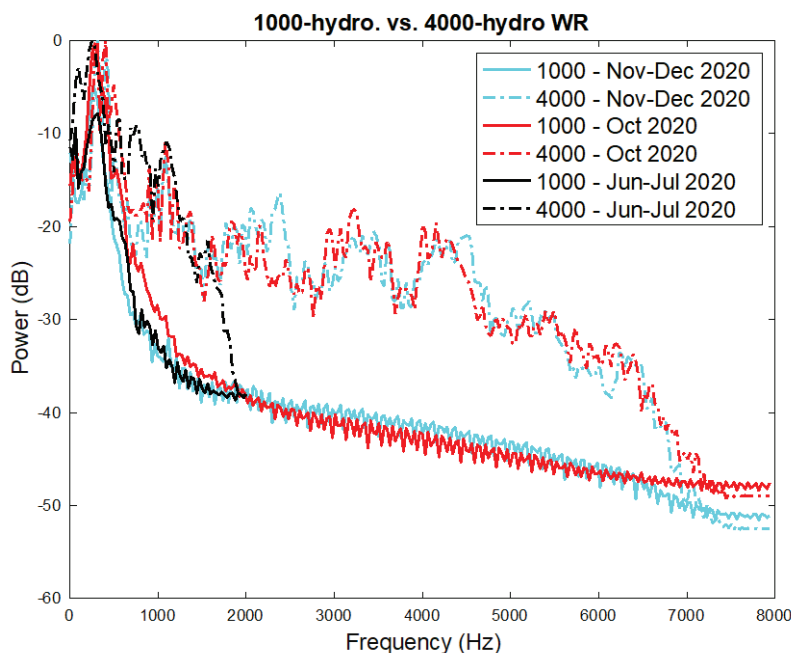
Figure 13. Power spectrum diagram showing the comparison of the frequency content obtained in lines 1000 and 4000 when shooting in the water reservoir. Note that the shorter curves for June-July 2020 campaign are due to the use of a slower sampling rate (0.25 ms) compared to the other campaigns (0.0625 ms).

Considering the same comparison of lines 1000 and 4000, but when shooting in the water reservoir (Figure 13), the results are opposite to what is observed in Figure 12. In this case, line 4000 shows higher frequency content in all the campaigns compared to line 1000. This is, most likely, related to better coupling in the reservoir than in the boreholes. The frequency content is higher when shooting in the reservoir compared to shooting in the shallow boreholes located within the dam (Figure 12). This higher frequency content increases the chances of imaging a defect within the core of the dam (Ivandic and Juhlin 2018).

3.3 IMAGING BY STACKING

In general, a straightforward seismic processing sequence was applied, as each hydrophone line was processed separately as a 2D line, without incorporating the data from the 3C-borehole geophone. Every type of data required different processing schemes related to the difference in frequency content due to the source position or the dam saturation status. For example, the frequency content is much higher when shooting in the water reservoir than from within the shallow boreholes located in the dam. Thus, the bandpass filter had to be adapted to the different frequency ranges of the collected data.

The most time-consuming processing step was the preparation of the data geometry that contained information about the shot IDs, receiver and source coordinates, and channels. Once this was complete a vertical stack of the repeated shot records was performed in order to increase the signal-to-noise ratio (usually ten shots per source point).

In order to obtain stacked sections of the hydrophone lines, a typical processing scheme was followed. Pre-stack processing steps were applied, such as assigning CDP geometry, automatic gain control (AGC, 100 ms) for increasing the amplitude of the seismic signals at far offsets, muting air waves (when shooting in the shallow boreholes), and bandpass filtering for reducing noise and focusing on the higher frequency band of the data (e.g. for line 1000 when shooting in the shallow boreholes a filter of 280-300-580-600 Hz was applied, and when shooting in the water reservoir a filter of 600-800-1800-2000 Hz). In some cases, Wiener deconvolution was applied for improving the signal-to-noise ratio. The data were stacked with constant velocities between 450-1300 m/s when shooting in the shallow boreholes, and 1800-2000m/s when shooting in the water reservoir. Stretch-mute and taper were important processes for imaging when shooting in the reservoir. A post-stack filter and balance were applied in most of the cases as final processing steps.

The reflection seismic processing results when shooting in the shallow boreholes (Figure 14 to Figure 18) show, in general, the same features. Similar structures can be recognized in each line for all the recording campaigns. Some residual noise is still present in some sections. Results for line 3000 (Figure 16) do not provide strong contrasts along the entire section. Signs of diffractions can be identified in lines 1000, 4000, and 5000 (Figure 14, Figure 17 and Figure 18) that could be related to the presence of defects in the internal structure of the dam.

The reflection seismic processing results when shooting in the water reservoir (Figure 19 to Figure 23) show also good consistency in the identified features along the recording campaigns. Noise and signals from reflections coming from the concrete wall are present at different locations. Lines 4000 and 5000 (Figure 22 and Figure 23) show higher frequency content in sections (b) and (c) due to the faster sampling rate compared to the one used in (a). Signs of a large diffraction are also identified in the central part of the lines in Figure 22 and Figure 23. Results from line 3000 (Figure 21) are of poorer quality compared to the other lines, probably due to the line not being completely inside the saturated zone.
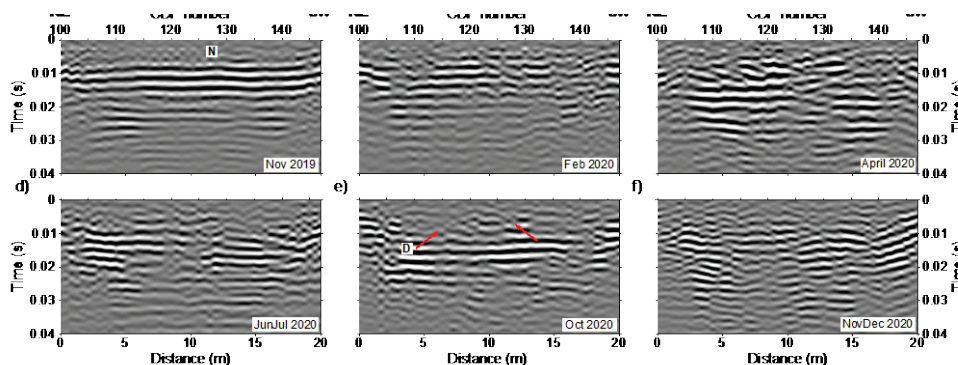

Figure 14. Reflection seismic processing results in line 1000, when shooting in the shallow boreholes, for the recording campaigns in (a) November 2019, (b) February, (c) April, (d) June-July, (e) October, and (f) November-December 2020. Labels D and N indicate signs of diffraction and noise, respectively.
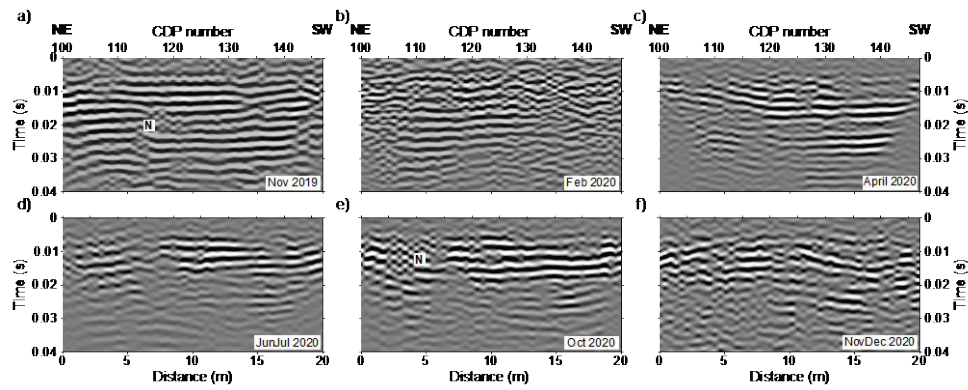
Figure 15. Reflection seismic processing results in line 2000, when shooting in the shallow boreholes, for the recording campaigns in (a) November 2019, (b) February, (c) April, (d) June-July, (e) October, and (f) November-December 2020. Label N indicates noise.
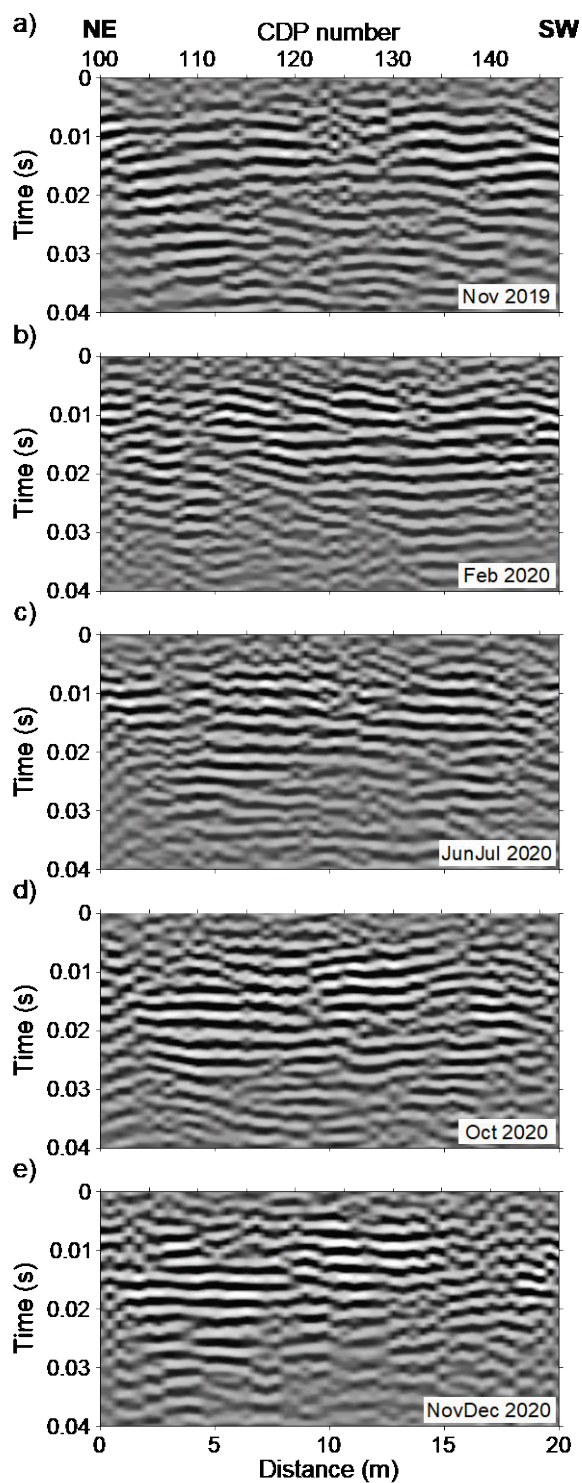
Figure 16. Reflection seismic processing results in line 3000, when shooting in the shallow boreholes, for the recording campaigns in (a) November 2019, (b) February, (c) June-July, (d) October, and (e) November-December 2020.
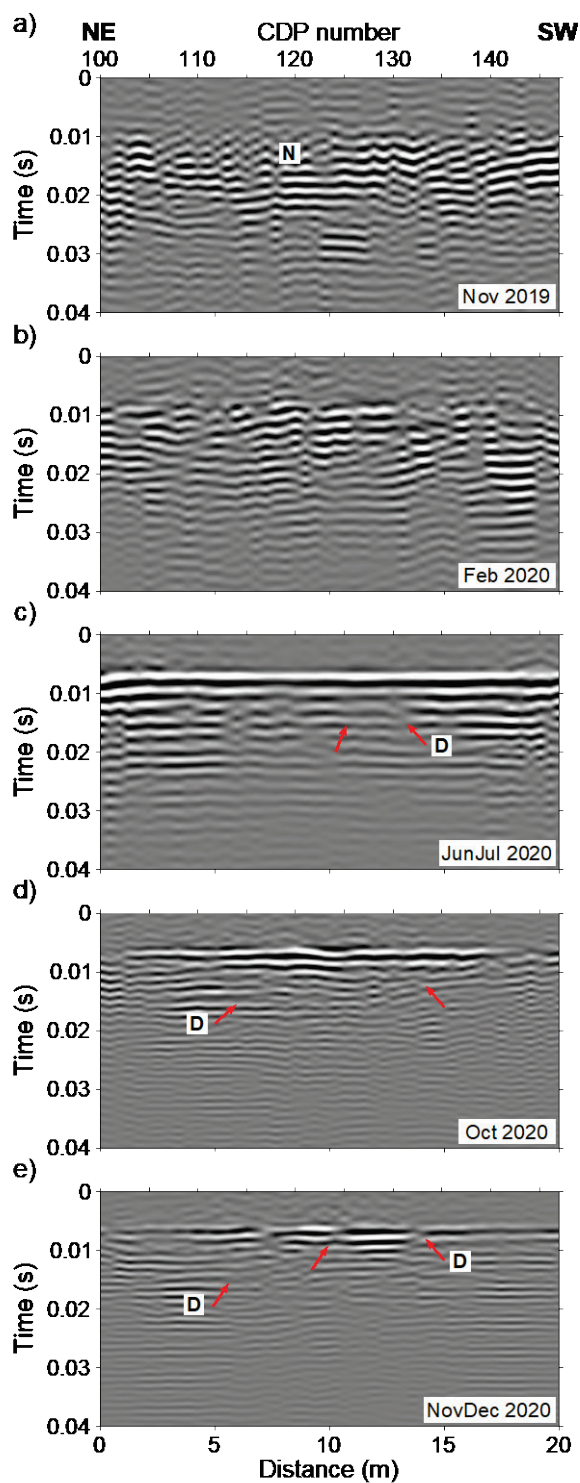
Energiforsk

Figure 17. Reflection seismic processing results in line 4000, when shooting in the shallow boreholes, for the recording campaigns in (a) November 2019, (b) February, (c) June-July, (d) October, and (e) November-December 2020. Labels D and N indicate signs of diffractions and noise, respectively.
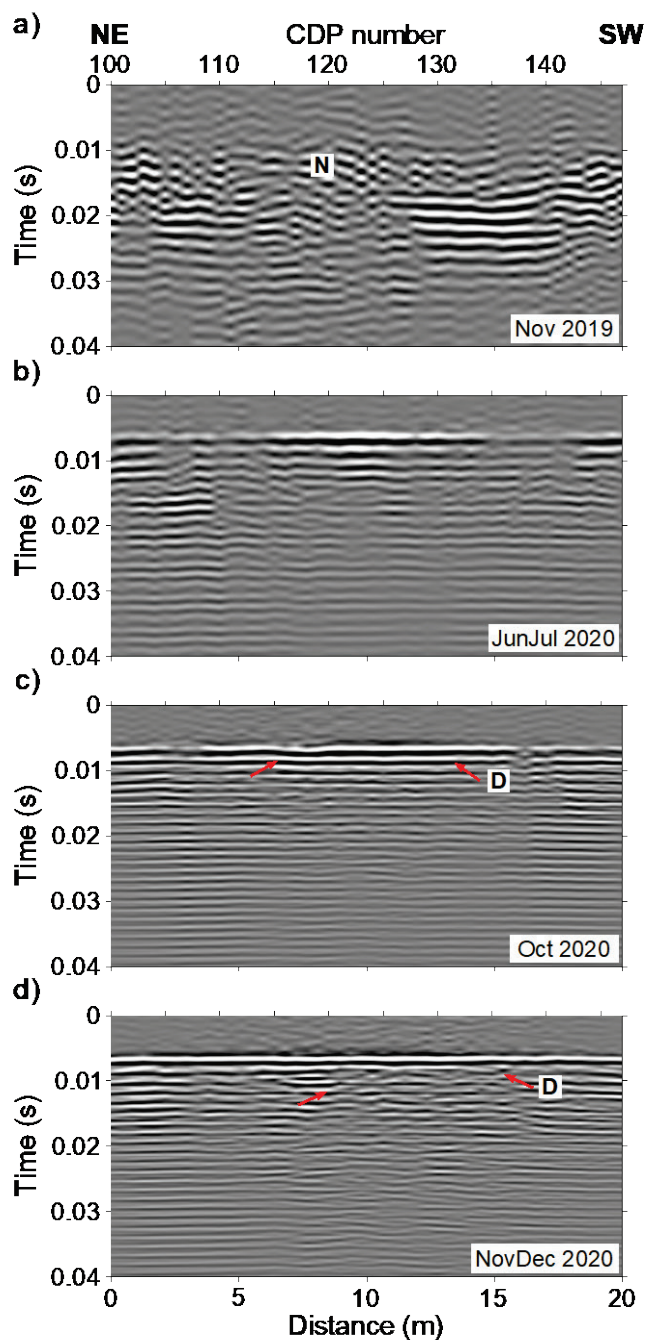
Figure 18. Reflection seismic processing results in line 5000, when shooting in the shallow boreholes, for the recording campaigns in (a) November 2019, (b) June-July, (c) October, and (d) November-December 2020. Labels D and N indicate signs of diffraction and noise, respectively.
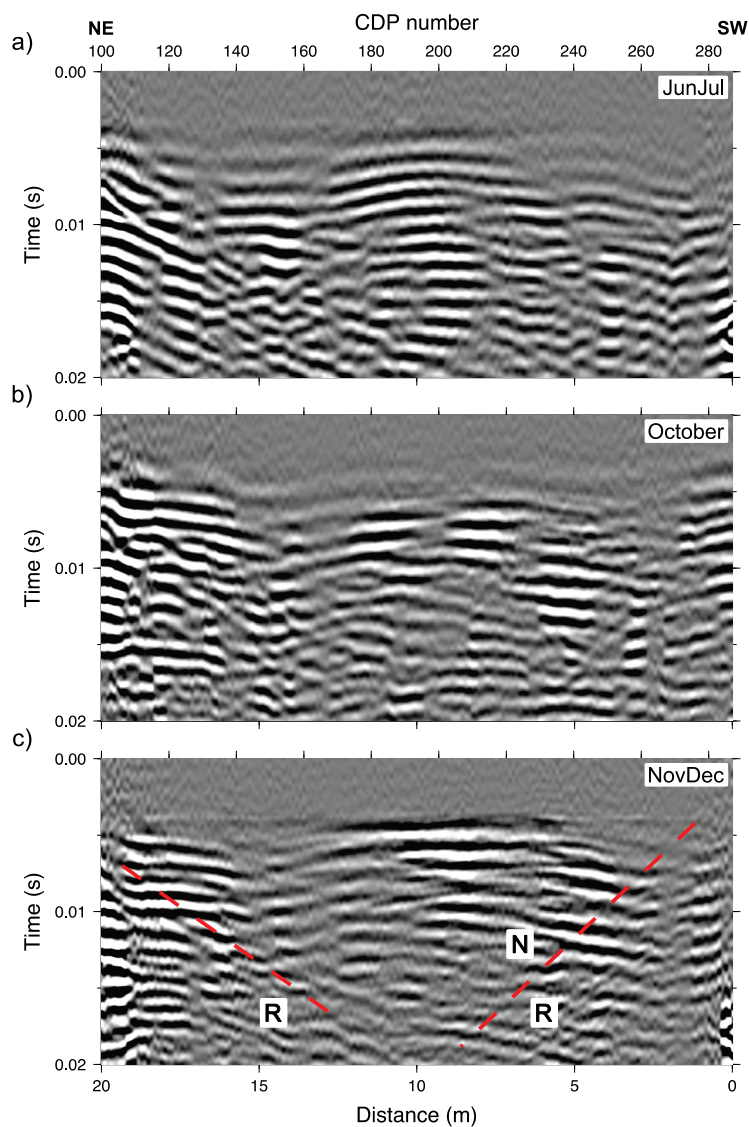
Energiforsk

Figure 19. Reflection seismic processing results in line 1000, when shooting in the water reservoir, for the recording campaigns in (a) June-July, (b) October, and (c) November-December 2020. Labels R and N indicate reflections coming from the concrete wall and noise, respectively.
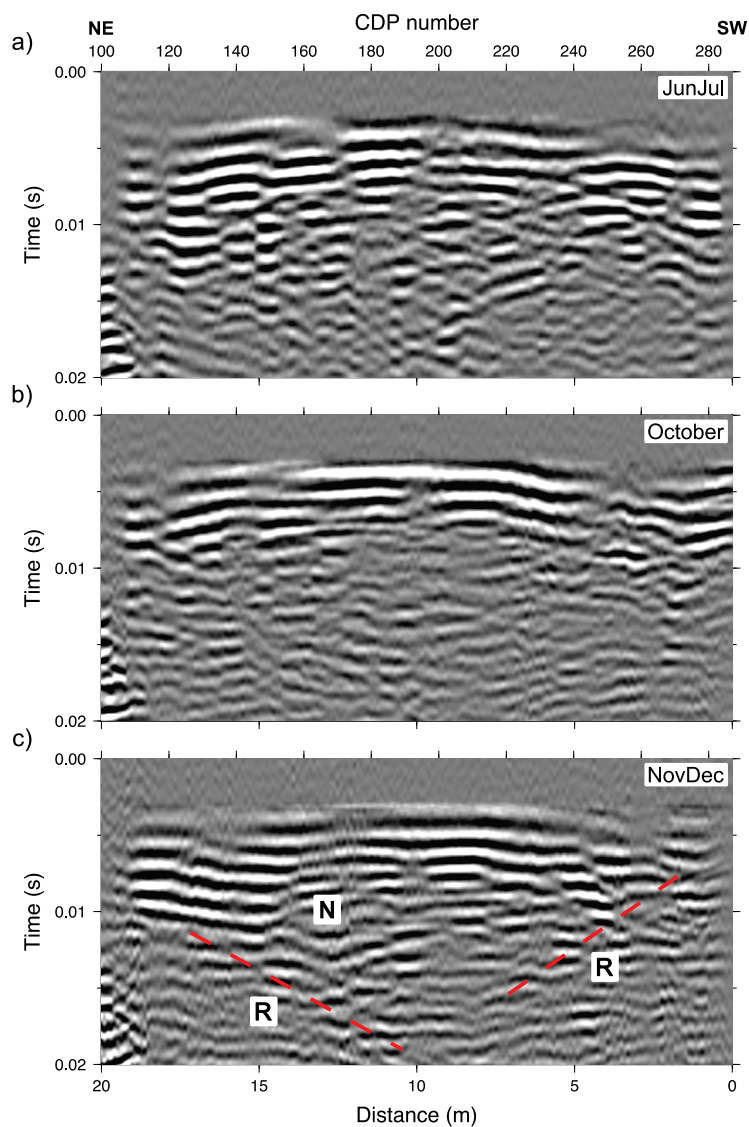
Figure 20. Reflection seismic processing results in line 2000, when shooting in the water reservoir, for the recording campaigns of (a) June-July, (b) October, and (c) November-December 2020. Labels R and N indicate reflections coming from the concrete wall and noise, respectively.
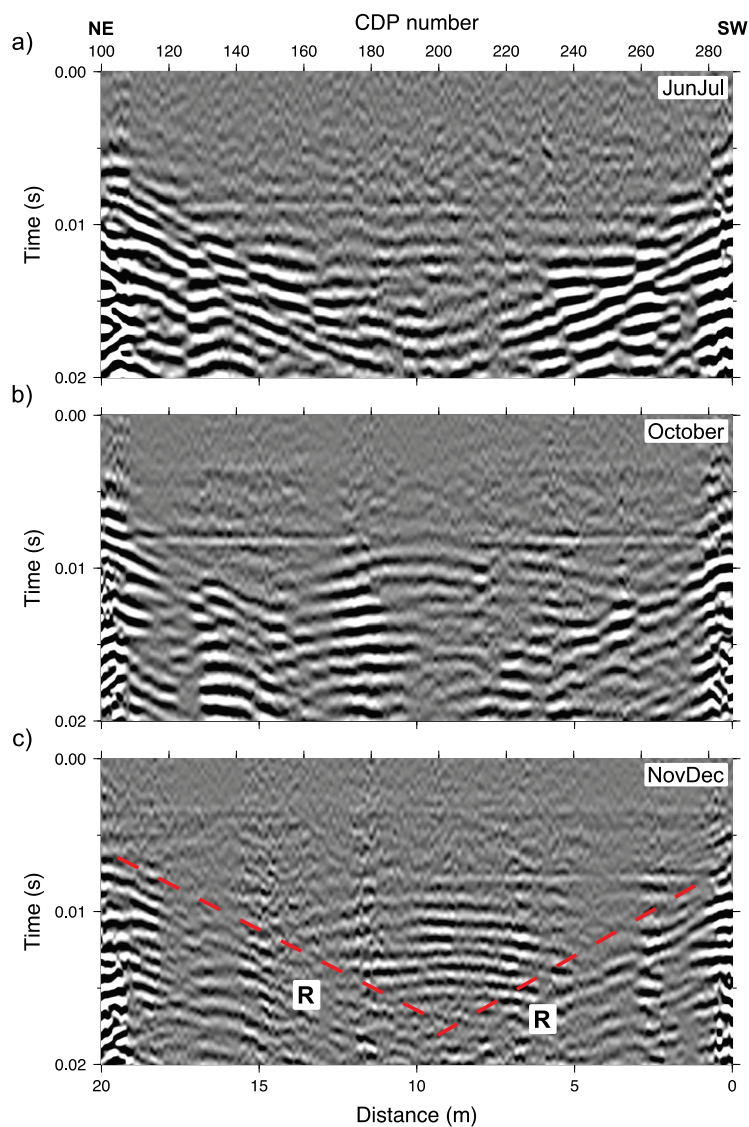
Figure 21. Reflection seismic processing results in line 3000, when shooting in the water reservoir, for the recording campaigns of (a) June-July, (b) October, and (c) November-December 2020. Label R indicates reflections coming from the concrete wall.
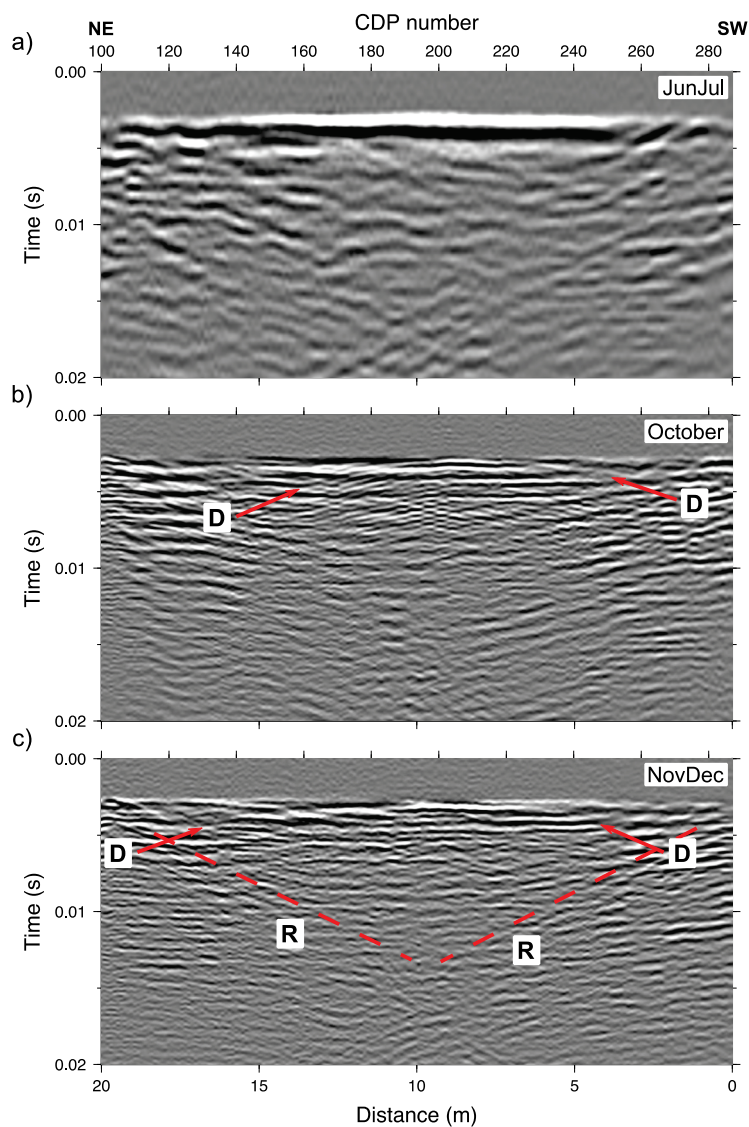
Figure 22. Reflection seismic processing results in line 4000, when shooting in the water reservoir, for the recording campaigns of (a) June-July, (b) October, and (c) November-December 2020. Labels R and D indicate reflections coming from the concrete wall and signs of diffraction, respectively. Note that a sampling rate of 0.0625 ms was used in October and November-December campaigns, compared to the sampling rate of 0.25 ms used in June-July campaign.
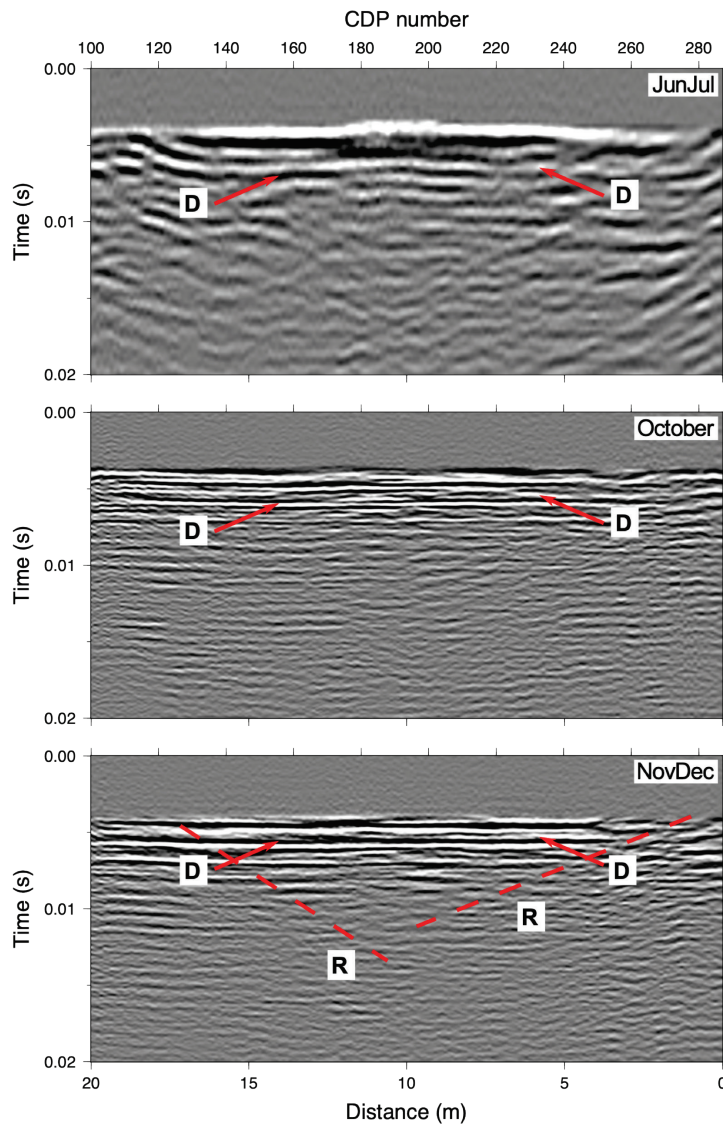
Energiforsk

Figure 23. Reflection seismic processing results in line 5000, when shooting in the water reservoir, for the recording campaigns of (a) June-July, (b) October, and (c) November-December 2020. Labels R and D indicate reflections coming from the concrete wall and signs of diffraction, respectively. Note that a sampling rate of 0.0625 ms was used in October and November-December campaigns, compared to the sampling rate of 0.25 ms used in June-July campaign.

3.4 ESTIMATES OF V_P AND V_S VELOCITIES AND POSSIBLE CHANGES WITH TIME

The results described here were obtained when estimating V_P and V_S using the data from the 3C-borehole geophone positioned inside one of the deep boreholes, and shooting in the rest of the deep and shallow boreholes installed in the experimental dam. We will refer to the different boreholes using the notation indicated in Figure 5. In order to estimate V_P and V_S, picking their arrivals (traveltimes) in the raw seismic data and calculation of the offsets were necessary. Then, averaged values for V_P and V_S, and other parameters as bulk and shear

modulus were calculated. In Table 1 an example from the data collected in the last field campaign, when the borehole geophone was positioned in BH6000 and the seismic source was used in BH8000 (see Figure 5 for exact locations), is shown. Both deep boreholes are located in the upstream side of the dam. The density of the core used in the calculations is 2090 kg/m³ (average value provided by Vattenfall).

Table 1. Data from November-December 2020, borehole geophone was in BH6000 and seismic source in BH8000.

Shot elevation (m)	Receiver elevation (m)	Approx. distance (m)	V_P (m/s)	V_S (m/s)	Bulk modulus (GPa)	Shear modulus (GPa)
25.39	26.2	19	450	114	0.38	0.027
22.99	23	19	1075	143	2.37	0.037

Table 1 shows that V_P increases by about 600 m/s from top to bottom of the dam structure. In contrast, V_S values are more similar and do not seem to be affected by elevation. If we now consider the data from previous campaigns (Figure 24) recorded in BH6000, BH7000 and BH8000 but shooting in the shallow boreholes located on top of the dam, we can observe two separate trends that, on average, correspond to approximately 200-300 m/s and 400-500 m/s. The data do not seem to be influenced by the deeper part of the core, but rather by the upper part where the velocities are lower. The two trends could be related to propagation through different materials or saturation areas. When recording in BH7000 (Figure 24b), the trends seem to be more clearly separated according to the recording campaigns. Lower velocities were registered in the last field campaign compared to the previous ones. This borehole shows a more progressive change in velocity, indicating a decrease in V_P with time.

Figure 25 compares pairs of different configurations of source and receiver for data collected in June-July (a) and (b), October (c) and (d), and November-December (e) and (f) 2020. Three types of data are compared, receiver in BH8000 and source in BH6000, receiver in BH8000 and source in BH7000, and receiver in BH6000 and source in BH7000 (see legend in Figure 25). The source elevation (four sampling points separated by 0.8 m distance) is indicated by the color code of the curves, with clearer colors for deeper positions within the hole. One can observe that the trend difference is larger in Figs. 30ace when compared to the results shown in Fig. 30bdf, mainly between 23.4 m and 25.5 m receiver elevation. This is probably related to the position of the boreholes and the average propagation velocity along the ray path trajectories between them. The distance, materials and degree of saturation in between are more similar when the receiver is in BH8000 and the source is in BH6000 or BH7000. In comparison, when the receiver is in BH6000 and the source is in BH7000, the distance is much smaller and the conditions may be different, too. In general, the trends indicate an increase in V_P at deeper positions within the hole and with time (V_P can reach up to 2400 m/s at the deepest position in Figure 25f). These high velocities may be due to the influence of the concrete floor of the dam.

Figure 26 shows the difference between the recording campaigns for each receiver-source configuration separately. Each curve represents a different source depth. In most of the cases, V_P increases at deeper source and receiver positions. In some positions in different configurations (Figure 26acef), the velocities show a clear increase with time. In other cases, like in Figure 26bd, the trends are similar between the different recording campaigns. In Figure 26bef the data show a decrease in the gradient between 24.5 and 25.5 m elevation from June-July to November-December 2020, maybe due to different saturation levels and/or other environmental factors, such as the change in temperature. Figure 26d also shows similar behavior between 23.5 and 24.5 m elevation. More accurate traveltime picking would improve the estimation of V_P and reduce the uncertainties in the data.
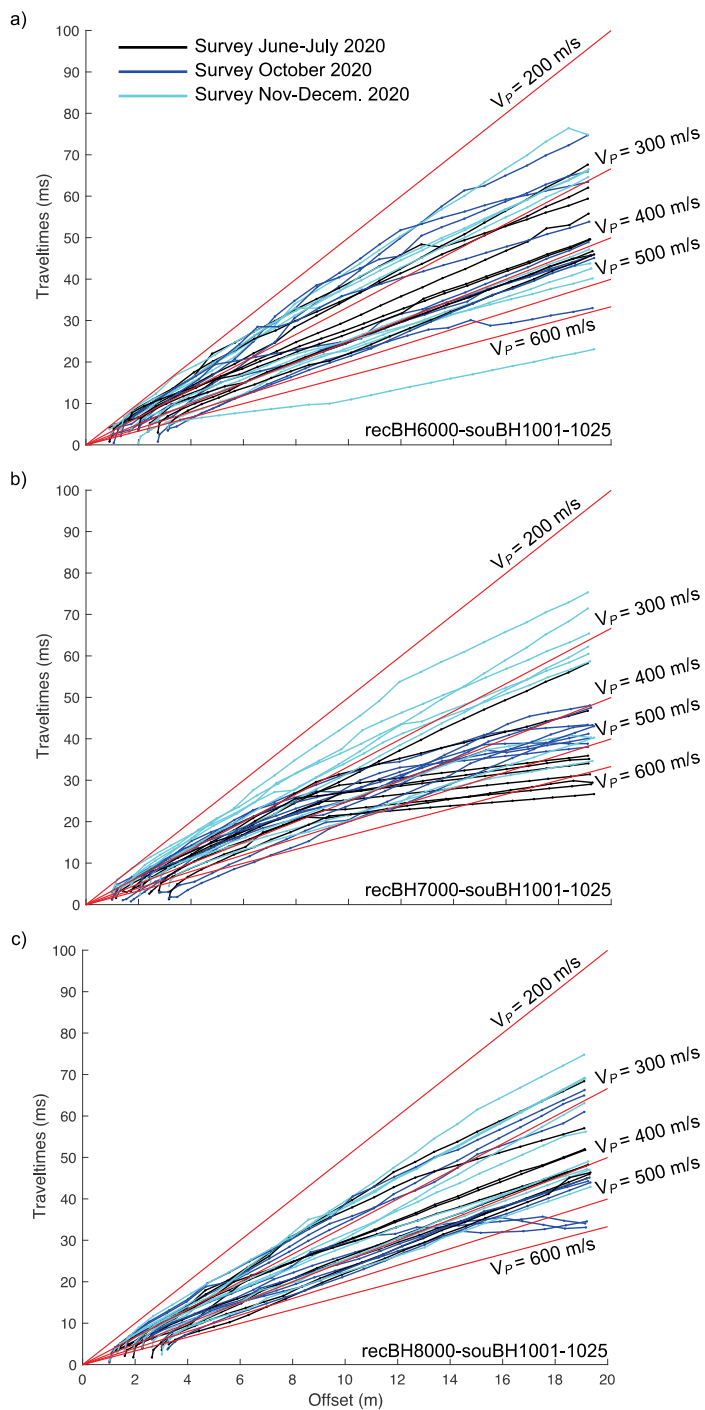
Figure 24. Offset versus traveltimes, when recording along (a) BH6000, (b) BH7000, and (c) BH8000, and shooting in the shallow boreholes on top of the dam, for three seismic surveys: June-July, October and November-December 2020. The red lines indicate slopes of constant velocity values.
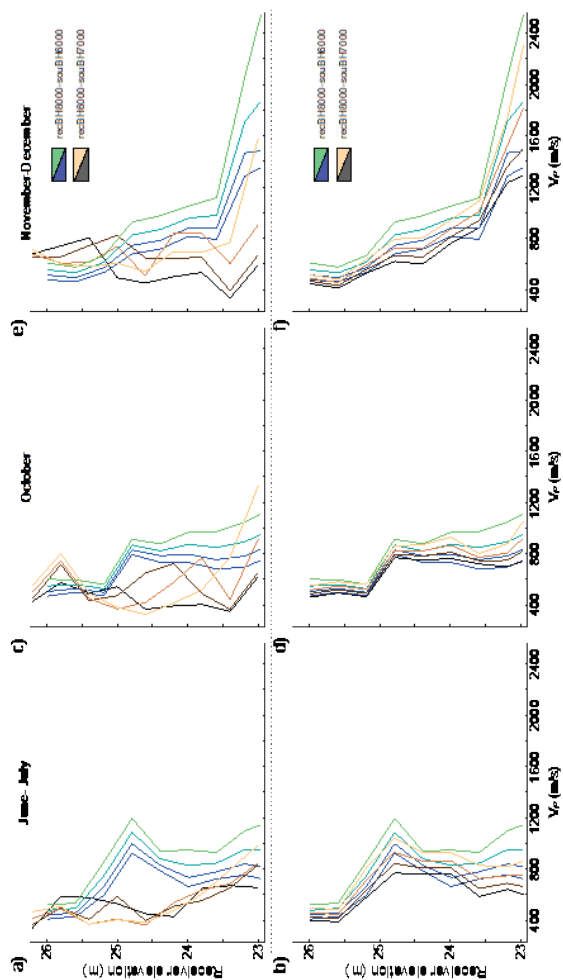
Figure 25. VP versus receiver elevation for data recorded in (a) and (b) June-July, (c) and (d) October, and (e) and (f) November-December 2020. The curves represent three datasets, data recorded in BH8000 but shooting in BH6000 or BH7000, and data recorded in BH6000 and shooting in BH7000 (see legend). The curve color indicates the source depth within the hole (four sampling points separated by 0.8 m), with clearer colors for deeper positions.
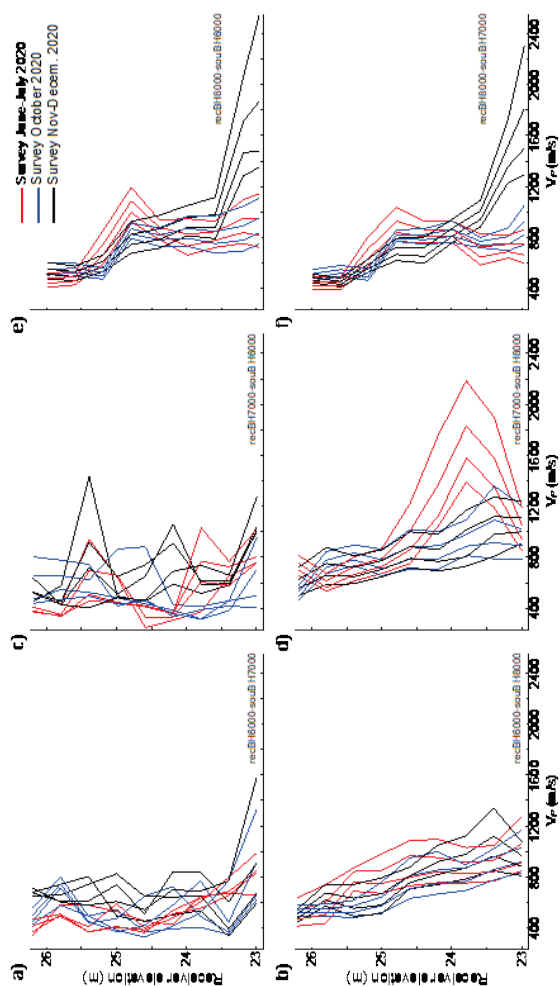
Figure 26. VP versus receiver elevation for (a) receiver in BH6000 and source in BH7000, (b) receiver in BH6000 and source in BH8000, (c) receiver in BH7000 and source in BH6000, (d) receiver in BH7000 and source in BH8000, (e) receiver in BH8000 and source in BH6000, and (f) receiver in BH8000 and source in BH7000. The color code indicates the different survey campaigns (see legend).

4 Seismic interferometry

4.1 ACTIVE SEISMIC INTERFEROMETRY

Imaging the subsurface is also possible using seismic interferometry. The method, used with active and passive data, is based on the cross-correlation of recorded seismic signals at different receivers for the retrieval of the Green's function (which contains information about the medium) of the waves propagating between the two receivers (Wapenaar et al. 2010). Some of the advantages of this method when dealing with complex systems are that it does not require previous knowledge of the subsurface velocity models, nor the real position of the source (see scheme in Figure 27).
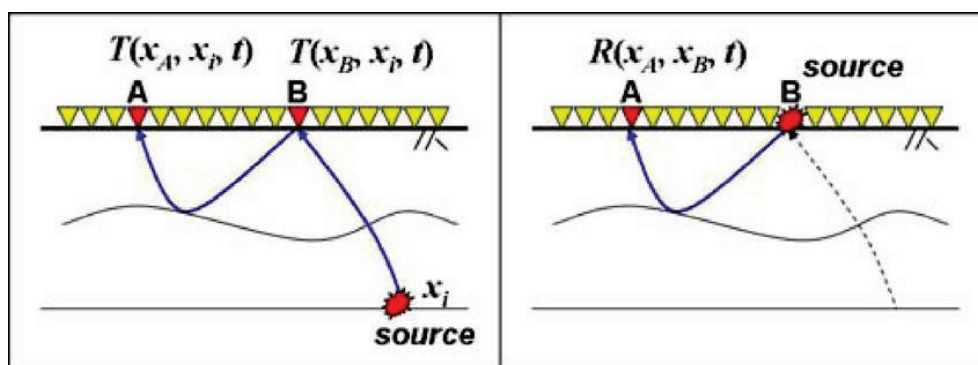

Figure 27.Seismic interferometry scheme (Matsuoka et al. 2008).

Seismic interferometry was tested on several lines. Here we present the results for two lines, line 4000 when shooting in the shallow boreholes (Figure 28), and line 1000 when shooting in the water reservoir (Figure 29). The procedure in both cases required saving the seismic response recorded in one receiver from the other line for the cross-correlation with all the receivers of the imaged lines.

For example, in the case of line 4000 (Figure 28) we tested all the seismic responses from each receiver of line 1000 (recorded in the same conditions), chose one and cross-correlated with all the receivers from line 4000. This test required to generate multiple stacks for choosing the one that provided the most coherent and improved results. Seismic responses for using the cross-correlation were provided in both lines from a receiver more or less located in the middle of the lines.

In Figure 28 and Figure 29, the comparison between the different methodologies shows slightly better results using seismic interferometry compared to the standard procedure (described in the section 'Imaging by stacking'). The main improvements are located in the upper parts of the sections, but the method also improved lower areas like in Figure 28b, where the diffraction event is sharper compared to the standard method.
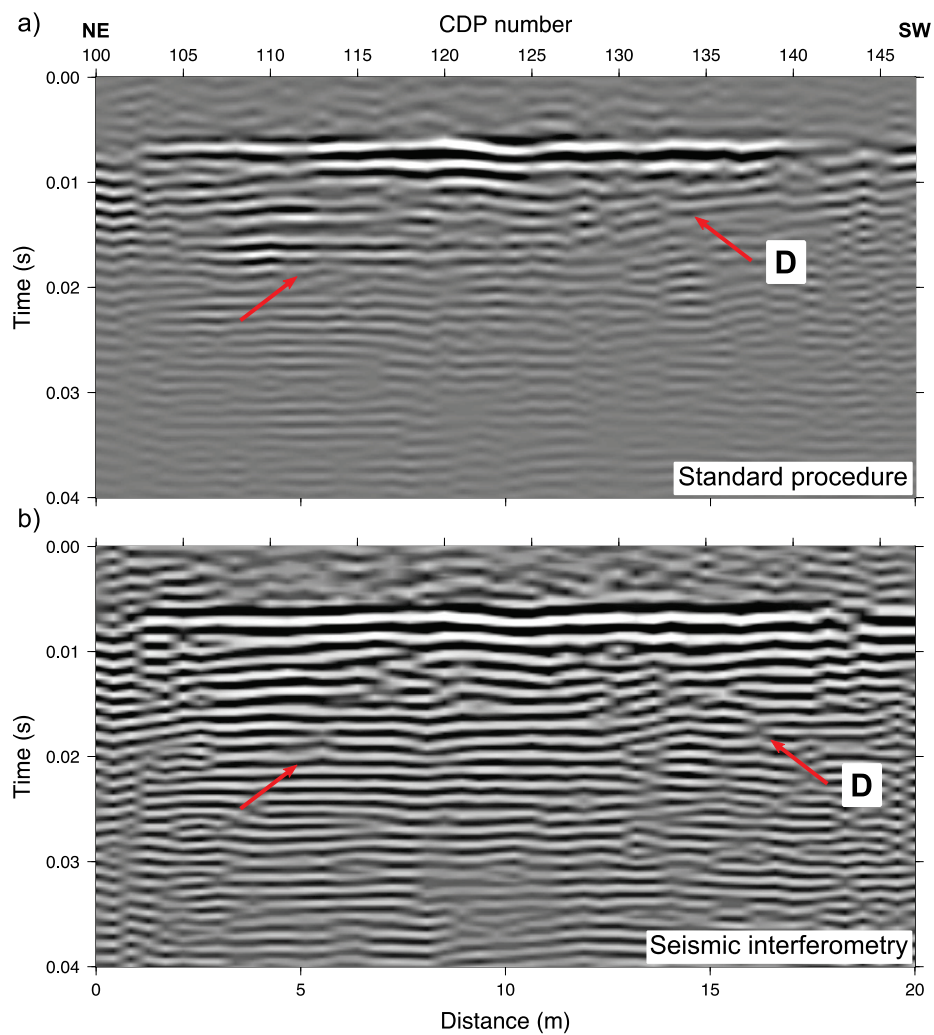
Figure 28. (a) Reflection seismic section of line 4000 (shooting in the shallow boreholes) processed using the standard procedure explained in 'Imaging by stacking'. (b) Same seismic section but processed using seismic interferometry. Signs of diffraction (D) are visible in both sections.
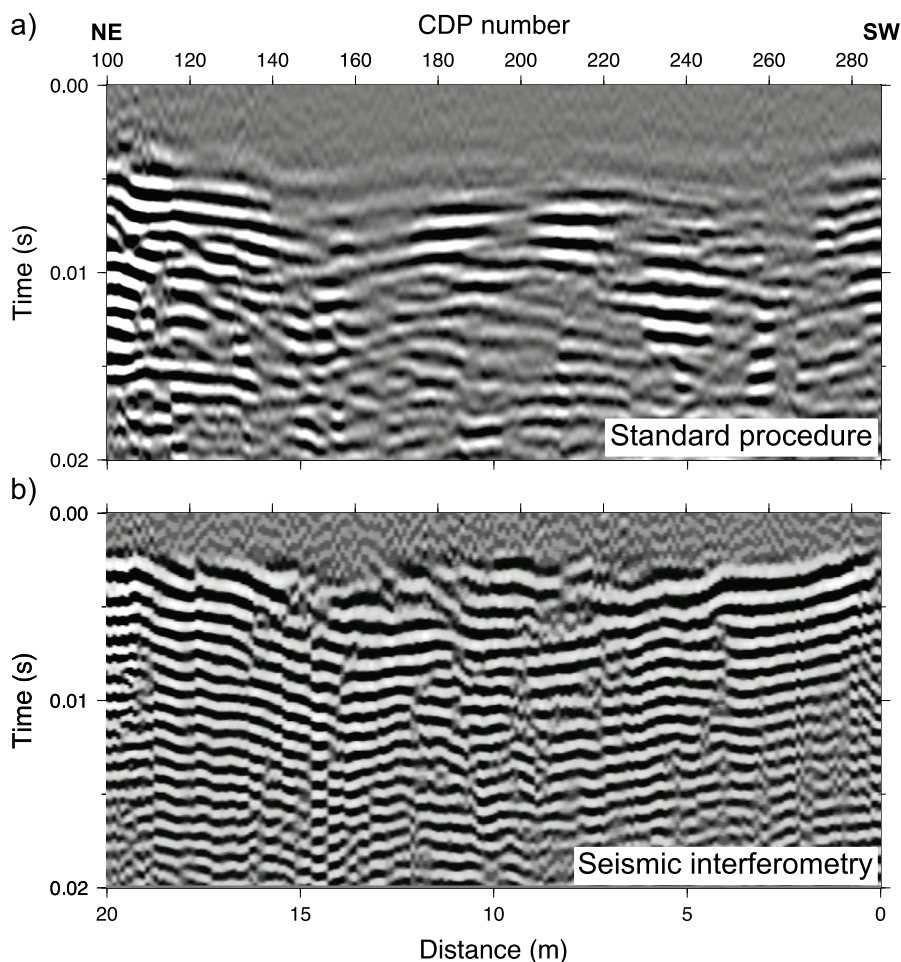
Energiforsk

Figure 29. (a) Reflection seismic section of line 1000 (shooting in the water reservoir) processed using the standard procedure explained in 'Imaging by stacking'. (b) Same seismic section but processed using seismic interferometry.

4.2 PASSIVE SEISMIC INTERFEROMETRY

Similar to active seismic interferometry it is possible to perform passive seismic interferometry using noise sources instead of active sources. One potential noise source are the defects in the dam itself. Water leaking through one of these defects could generate seismic waves that can theoretically be observed on the passive recordings. By repeated recordings, cross correlation and stacking, the location of the source can potentially be determined. For this methodology to work would require that the signals from the defect have an amplitude on the order of other noise sources near the dam, such as pumps, generators, etc. This is highly unlikely. Figure 30 shows a typical example of part of a 4 s long recording from December 2020. The three panels show the same data, but without any filtering, after notch filtering 50, 100 and 150 Hz noise and after bandpass filtering. Raw data show essentially electronic noise. After notch filtering there are clear signs of waves propagating along line 2000 (top sensors upstream) in both directions. These have peak frequencies of about 12 Hz and an apparent velocity of about 200 m/s. After bandpass filtering, coherent higher frequency waves are also observable that

propagate along lines 4000 and 5000 with apparent velocities of about 500-600 m/s. In contrast to the lower frequency waves on line 2000, these waves seem to propagate only from right to left across the arrays (from south to towards north).
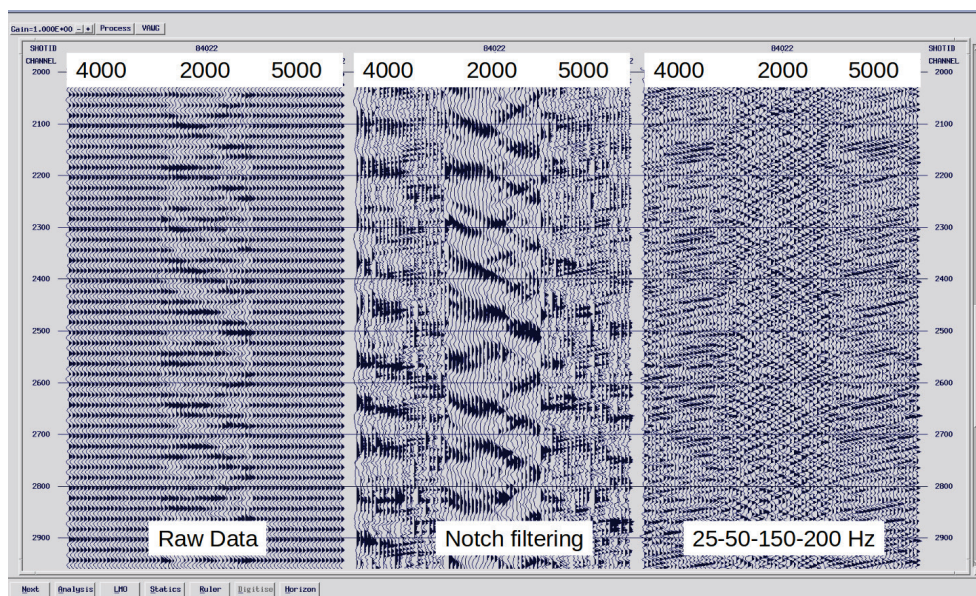

Figure 30. Part of a 4 second record showing typical data from Lines 4000, 2000 and 5000 in December 2020.

Figure 31 shows part of a 4 s record (plotted with the same parameters as in Figure 30), but with a stronger noise burst present. Bursts such as these are present on perhaps 5% of the records, but not at regular intervals. Note that the noise arrives first on the right-hand edge of line 5000 (in the south) and propagates northward on all three lines. On line 5000 the noise lines up almost along a straight line, but on line 4000 there is some curvature. It is difficult to judge the linearity of the noise on line 2000, but it appears to arrive later than on both lines 4000 and 5000. The observation that noise arrives first on line 5000 and seems to propagate with a constant velocity along the line suggests that the noise source is close to the continuation of line 5000 to the south. Apparent velocities of the noise burst waves on line 5000 are also around 500-600 m/s.
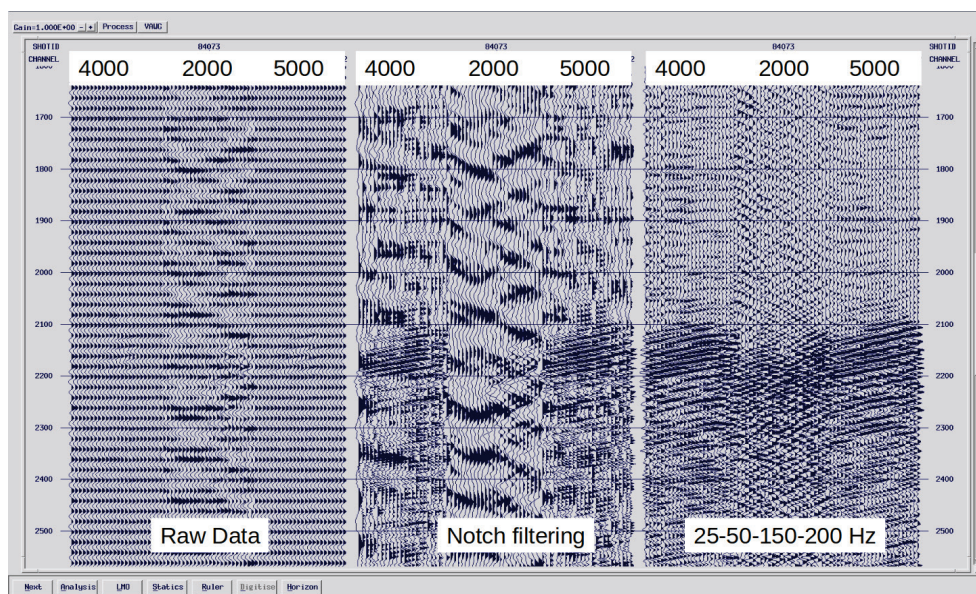
Figure 31. Part of a 4 s record showing a strong noise burst on Lines 4000, 2000 and 5000 in December 2020.

By cross-correlating the data with a selected channel an apparent virtual source gather may be created in which the resulting seismograms may be viewed as having the source at the position of the selected channel. Cross-correlations for the data shown in Figure 30 and Figure 31 are shown in Figure 32 and Figure 33, respectively, along with cross-correlations with adjacent data records. The cross-correlations show that the two resulting data records are very similar in spite of the noise burst being much stronger. This is because the typical signal is very repetitive and the lower amplitudes are compensated by more events in a record, resulting in correlations that do not differ much. The main controlling factor for the correlation output is the level of the noise relative to the electronic noise. For example, the leftmost panel in Figure 32 shows mainly correlation of electronic noise (arrival times are the same on all channels). Apparent velocities of the correlated events on line 5000 are about 550 m/s. Some curvature is also seen on line 4000, but with an asymptotic velocity of about 550 m/s. The less well correlated events on line 2000 have a velocity of about 200 m/s.

The signal-to-noise ratio of the virtual source gather can be improved by stacking the cross-correlated records generated for the selected channel. Figure 34 shows results from stacking the first 800 records and stacking all 10400 records. Stacking of 800 records improves the coherency of the main events compared to the electronic noise. Stacking all records further improves the signal-to-noise ratio. On line 5000 the event has an apparent velocity of about 550 m/s. The less coherent events on line 2000 have an apparent velocity of about 200 m/s.

It is interesting to plot the response at a single channel after cross-correlation as a function of time (Figure 35). There is a clear periodicity in the response with higher amplitudes in 4-5 traces of the cross-correlation about every two minutes, or a little less than this. This response strongly suggests some mechanical source for the noise on the south side of the dam close to the end of line 5000.

Energiforsk

Figure 32. Four records from the December 2020 passive data after cross-correlation with channel 65 and shifting the results to 50 ms. The second panel from the left shows the cross-correlation for the data in Fig. 35 after filtering.
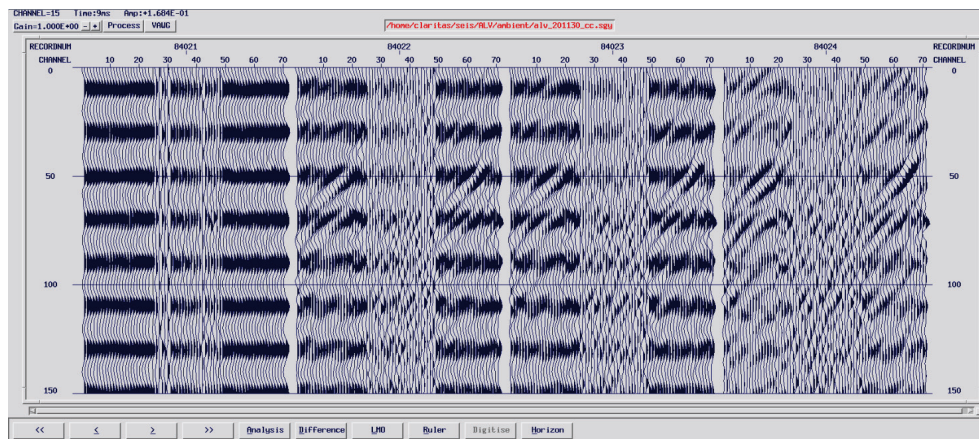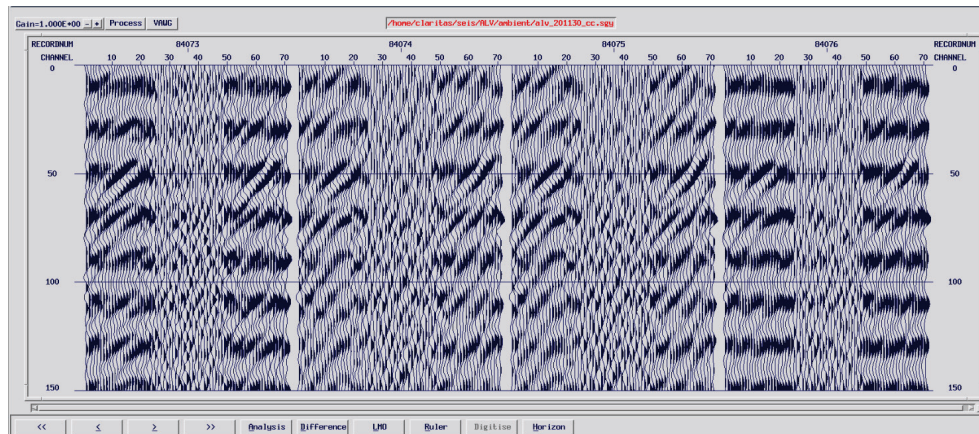

Figure 33. Four records from the December 2020 passive data after cross-correlation with channel 65 and shifting the results to 50 ms. The first panel from the left shows the cross-correlation for the data in Fig. 36 after filtering.

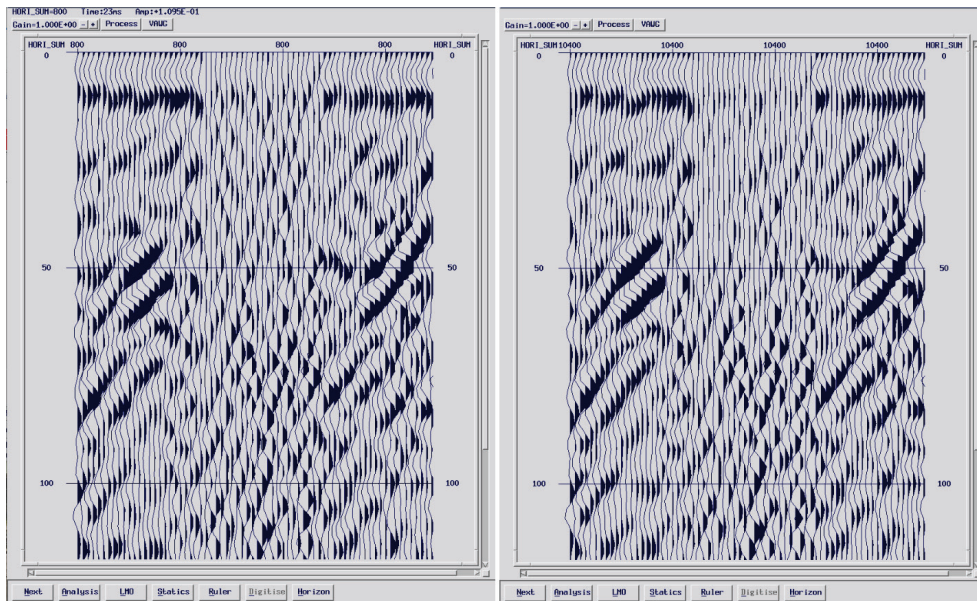**Figure 34. Results from stacking the cross-correlations. Panel on the left shows results from stacking the first 800 cross-correlated records. Panel on the right shows results from stacking all 10400 records.**
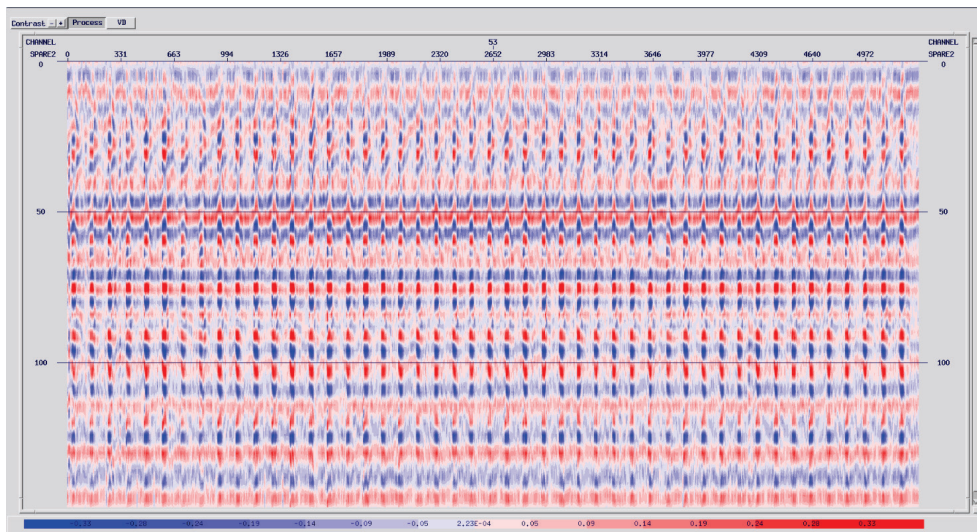

Figure 35. First 800 cross-correlation records from channel 53. Total time corresponds to about 90 minutes of data. Note the repetitive pattern with stronger amplitudes occurring on 4-5 traces about every 2 minutes.

5   P-wave traveltime tomography

P-wave traveltime tomography (using the tomography algorithm PStomo_eq by Tryggvason et al. 2002) was tested in order to check the validity of the method for detecting defects within the dam structure. This method is based on the inversion of picked traveltimes (first arrivals) for imaging the velocity structure of the subsurface (see Figure 36).

In this study both synthetic and real data were used as input for the traveltime tomography. The ability of traveltime tomography to recover the defects is greatly influenced by the defect's position in relation to the seismic ray coverage. Sparse ray coverage in some parts, such as the central lower part of the dam, limited imaging of defects in these parts. A defect located closer to the top hydrophone lines or one of larger size, would generally produce better defined anomalies, easier to identify.
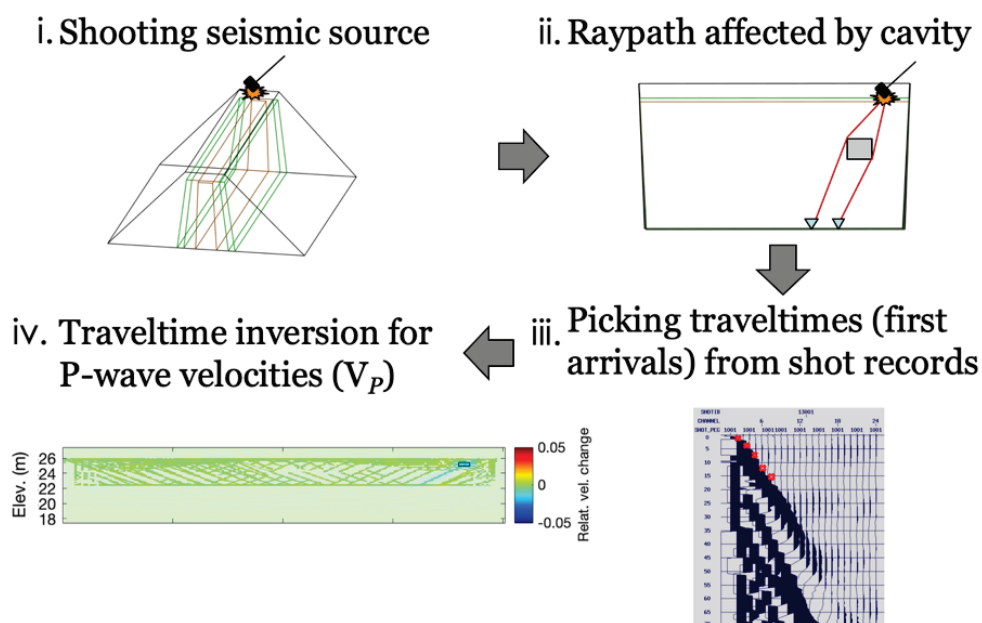
Figure 36. Overview of the scheme followed by the P-wave traveltime tomography method for detecting a cavity.

5.1   TOMOGRAPHIC SYNTHETIC MODELING

Synthetic traveltimes were generated considering a P-wave velocity structure of the dam and the geophysical acquisition design. The velocity model for generating synthetic traveltimes was based on the one by Ivandic and Juhlin (2018) and consists of the dam being filled with water up to a height of 3.5 m. The material velocities differ for providing enough contrast between the different materials, for example, the inner core and the foundation (concrete and underlying materials) velocity are 3000 and 5000 m/s, respectively. Within the dam, different defects were modeled as cavities or permeable/loose layers (low velocity zones with varying

size and position). Other factors like noise or error in the acquisition geometry were also added. For the inversion, a cell size (x, y, z) of 0.1 m^3 was used. The starting model was (see dam geometry in Figure 2): A – 3000 m/s, B – 2200 m/s, C – 1800 m/s, D – 2000 m/s, foundation – 5000 m/s, water – 1500 m/s, and air – 340 m/s. The inversion was run for nine iterations with decreasing smoothing parameter. Two of the tested defect designs (cases) are presented below.

Case 1: cavity

Size: 0.4 m^3 & V$_P$ = 1000 m/s

Figure 37. Synthetic P-wave traveltime tomography results for cross sections (a) across, XZ, and (b) along, YZ, the dam at 18.20 and 7.50 m distance in y- and x-direction, respectively. From top to bottom the accumulated ray length per cell, the inverted V$_P$ model, and the relative velocity change of the inverted velocity model with respect to the starting model are shown in each cross section. The position of the modeled cavity is represented by a black solid box. Note that the solid colors indicate cells crossed by ray paths.

Case 2: horizontal permeable layer

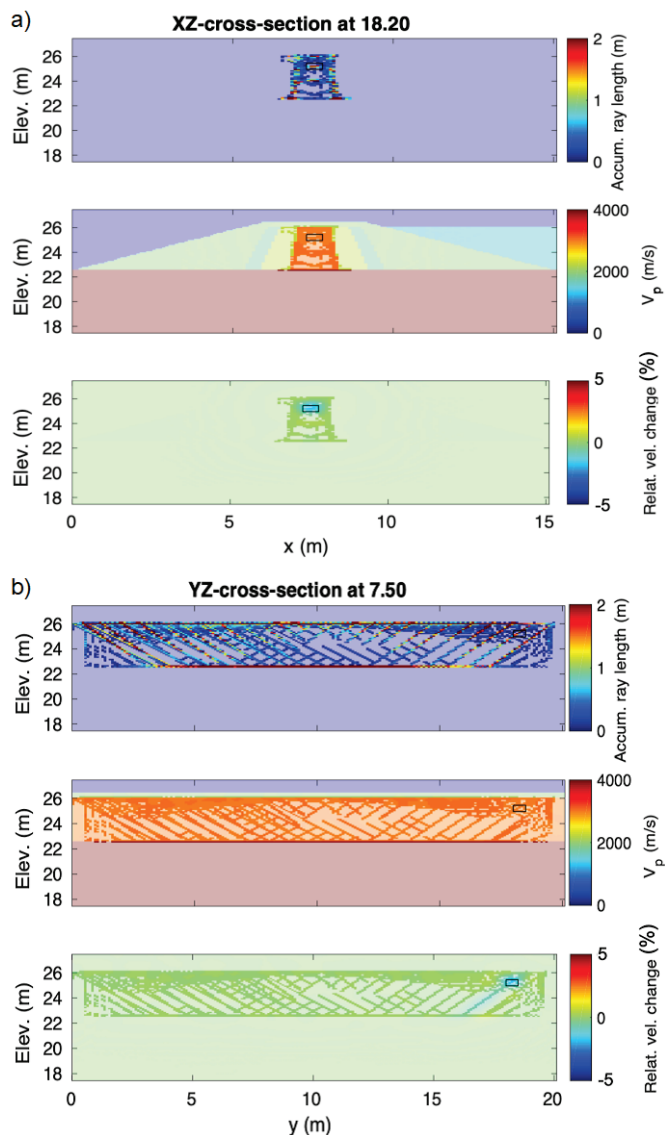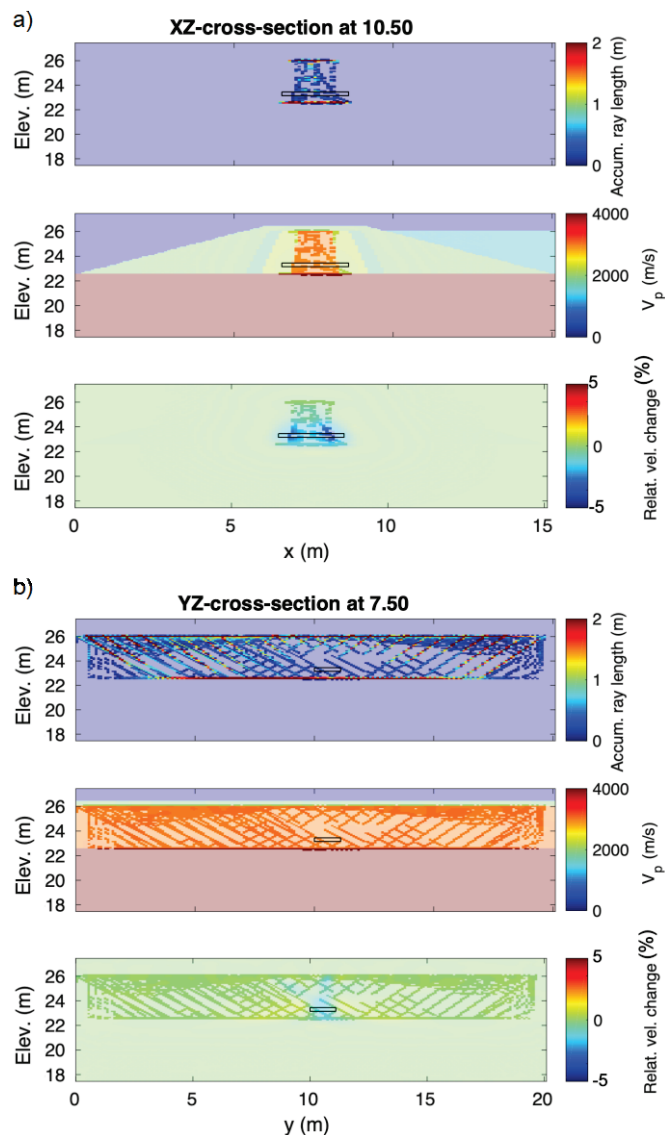Size: 2 x 1 x 0.4 m³ & V$_P$ = 1000 m/s

Figure 38. Synthetic P-wave traveltime tomography results for cross sections (a) across, XZ, and (b) along, YZ, the dam at 10.50 and 7.50 m distance in y- and x-direction, respectively. From top to bottom the accumulated ray length per cell, the inverted V$_P$ model, and the relative velocity change of the inverted velocity model with respect to the starting model are shown in each cross section. The position of the modeled horizontal permeable layer is represented by a black solid box. Note that the solid colors indicate cells crossed by ray paths.

The results of the synthetic modeling in Figure 37 and Figure 38 show, in general, that the defect positions can be identified. The velocity and size of the defects, however, are not well recovered by the method. Few rays pass through the defects and the inverted velocity models do not show anomalies at the defect positions. The relative velocity change, however, shows a negative anomaly where the defects are located and a smearing out along the ray paths (Figure 37b and Figure 38ab). Note that the relative velocity change values are very small (ca. 2 %), which may be too small when identifying the defects using real data.

Energiforsk

In order to approach the problem from a more realistic perspective, a second velocity model was produced mostly based on the estimated V_P values using first arrival information. The data from different campaigns indicate that the dam structure is probably not fully saturated in the top part of the dam, but partially or completely unsaturated at the three top hydrophone lines (1000, 2000 and 3000). Thus, it was necessary to incorporate an unsaturated area above the water level in the reservoir (c. 3.2 m above the bottom part of the dam) with lower velocities. For the inversion, a cell size (x, y, z) of 0.1 m^3 was used. The starting model was divided in saturated and unsaturated materials according to Table 2, with additional velocities being: foundation 3500 m/s, water 1500 m/s, and air 340 m/s. The defect was a cavity located in the middle of the dam, of size 0.4 m^3 and V_P of 600 m/s. The inversion was run for nine iterations with decreasing smoothing parameter.

Table 2. Second starting model for synthetic P-wave traveltime tomography.

	A	B	C	D
Saturated material	1600 m/s	1300 m/s	1000 m/s	800 m/s
Unsaturated material	500 m/s	400 m/s	300 m/s	250 m/s

Figure 38 shows the results of the synthetic modeling using this, more realistic velocity model. (a) and (b) present the results when only the sources located in the shallow/deep boreholes are used, and (c) and (d) include also the results when shooting in the water reservoir. Recording is in the deep boreholes and on the hydrophone lines. As observed before in the previous figures, the velocity and size of the cavity are not well recovered by the method. The ray coverage is low at the cavity location and a negative anomaly is only visible at the defect position in the relative velocity change results (third window starting from the top in Fig. 44abcd). The smearing out along the ray paths, observed in Figure 36 and Figure 37, is also visible here. Note that the relative velocity change values are very small (c. 0.2-0.5 %).
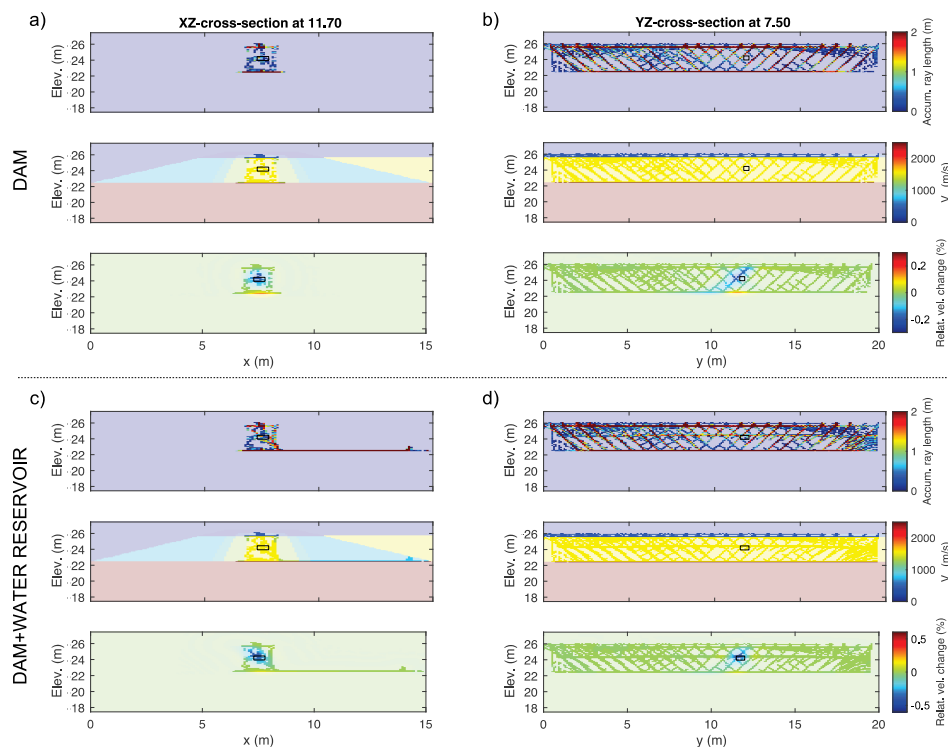
Figure 39. Synthetic P-wave traveltime tomography results for cross sections (a) (c) across, XZ, and (b) (d) along, YZ, the dam at 11.70 and 7.50 m distance in y- and x-direction, respectively. From top to bottom the accumulated ray length per cell, the inverted V_P model, and the relative velocity change of the inverted velocity model with respect to the starting model are shown in each cross section. The position of the modeled cavity is represented by a black solid box. Note that the solid colors indicate cells crossed by ray paths.

5.2   REAL DATA TOMOGRAPHY

Traveltimes from three recording campaigns were available, June-July, October and November-December 2020, both crosshole recordings and on the hydrophone lines. We decided to invert the data in two ways, one just considering the data when shooting in the shallow/deep boreholes, and the other one considering all the data, i.e. when shooting in the shallow/deep boreholes and in the water reservoir. Multiple starting models were tested in order to better adjust the data to the available materials. A similar approach as the one used for the realistic synthetic modeling above (see also Figure 39), with an unsaturated zone above the water level, was preferred. Table 3 shows the chosen starting model when shooting only in the shallow/deep boreholes, and Table 4 shows the chosen starting model when shooting in the shallow/deep boreholes and in the water reservoir.

Table 3. Starting model for synthetic P-wave traveltime tomography when shooting in the shallow/deep boreholes. Foundation velocity is 1100 m/s, water is 1500 m/s and air 340 m/s.

	A	B	C	D
Saturated material	1000 m/s	800 m/s	650 m/s	500 m/s
Unsaturated material	500 m/s	400 m/s	350 m/s	300 m/s

Table 4. Starting model for synthetic P-wave traveltime tomography when shooting in the shallow/deep boreholes and in the water reservoir. Foundation velocity is 1100 m/s, water is 1500 m/s and air 340 m/s.

	A	B	C	D
Saturated material	1300 m/s	1100 m/s	1000 m/s	800 m/s
Unsaturated material	500 m/s	400 m/s	350 m/s	300 m/s

For the inversion, a cell size (x, y, z) of 0.2 m³ was selected because it provided a less sparse ray coverage than 0.1 m³. Fixing the velocity of the foundation, water and air was also important in keeping most of the ray paths within the dam structure. The inversion when shooting in the shallow/deep boreholes was run for 11 iterations, and 9-10 iterations when shooting in the shallow/deep boreholes and in the water reservoir. A decreasing smoothing parameter was applied in combination with a residual error threshold, selecting only traveltime data with a residual error below the threshold in each iteration. Fixing this threshold stabilized the inversion for both cases, starting with a low number and increasing in consecutive iterations, allowing more data to be incorporated in the inversion. We observed that there is a part of the data that produces higher residuals for the chosen starting models. This suggests that the picked traveltimes may have some error at larger offsets, and/or most probably the starting models do not constrain well enough the data at larger offsets. We believe that the larger offset data are related to picked traveltimes at the deeper positions in the deep boreholes (BH6000 to BH9000). For example, when shooting in BH8000 and recording in BH6000.

Figure 40 shows the results of the inversion when shooting in the shallow/deep boreholes. Each view shows the accumulated ray length per cell (ray coverage) on top and on the bottom the inverted V_P model for three recording campaigns, June-July (Figure 40abc), October (Figure 40def) and November-December (Figure 40ghi) 2020. From the results we can observe that, with some exceptions, all the ray paths concentrate in the dam structure. The inverted V_P values in the core range mostly between 400 and 600 m/s, in the top unsaturated part V_P is below 500 m/s, and the foundation velocity remains around 1100 m/s. The velocity values increase slightly with time. The core velocity is lower than expected for a compacted saturated clay (1800-2200 m/s), thus these values are at odds with expectations. The velocity models are similar for the three recording campaigns, showing higher velocities in the core and lower above and below (the velocity decreases again at the bottom central part of the dam, YZ-cross sections in Figure 40beh). This may be

related to the presence of low velocities in this area in the dam or it may indicate that this part of the model is poorly constrained.

Figure 41 shows the results of the inversion when shooting in the shallow/deep boreholes and in the water reservoir. As in Figure 40, each view represents on the top the accumulated ray length per cell and on the bottom the inverted V_P model for three recording campaigns, June-July (Figure 41abc), October (Figure 41def) and November-December (Figure 41ghi) 2020. Compared to the data in Figure 40, all the ray paths are concentrated in the dam structure, with some of them extending into the water reservoir connecting to the source locations there. The inverted V_P values in the core now range between 600 and 900 m/s, in the top unsaturated part V_P is below 600 m/s, and the foundation velocity remains around 1800 m/s. At the base of the dam, the velocities are higher than 1300 m/s, and at the position of the deep boreholes, the velocities are lower compared to the rest of the model. The core velocity, although smaller than expected, is higher with respect to the previous models shown in Figure 40. Thus, adding the water reservoir traveltimes seems to constrain better the inversion and keeps the velocities in the core within a more realistic range. The V_P models in the YZ-cross sections in Figure 41beh and XY-cross section in Figure 41i, show possible low velocity zones in the core between 22 and 24 m elevation. These low velocity zones are located at 8 and 15 m distance in Figure 41h. These zones could be related to potential defects or a poorly constrained model in these areas.
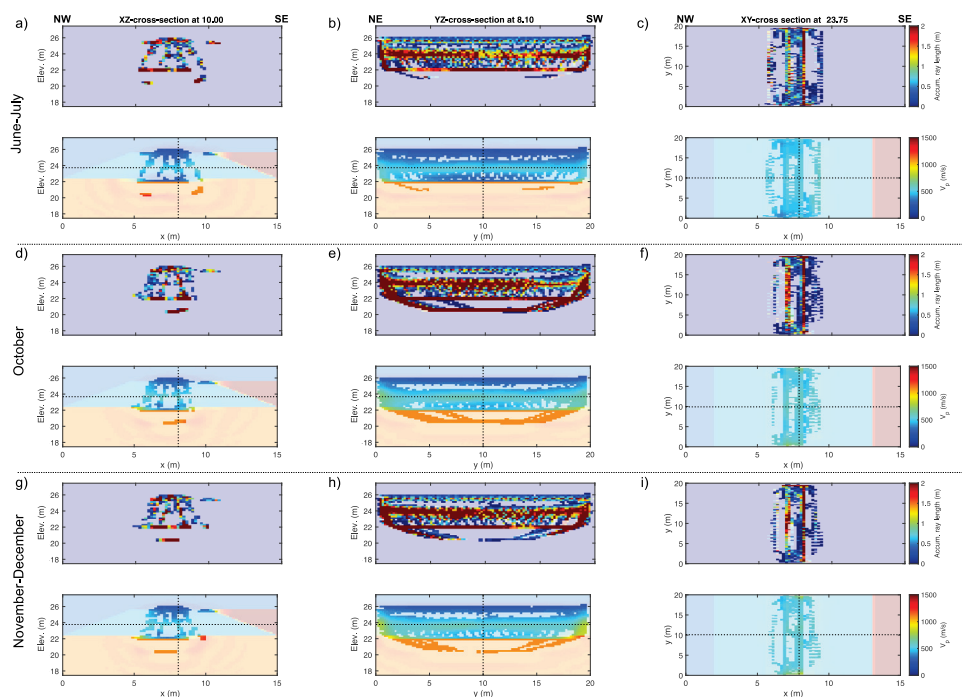

Figure 40. Real P-wave traveltime tomography results when shooting in the shallow/deep boreholes for cross sections XZ, YZ and XY across and along the dam for recording campaigns in (a) (b) (c) June-July, (d) (e) (f) October, and (g) (h) (i) November-December 2020. From top to bottom the accumulated ray length per cell, and the inverted V_P model are shown in each cross section. Note that the solid colors indicate cells crossed by ray paths. The straight lines represented in the V_P model indicate the position along the x- and y-axis, and elevation of each cross section.
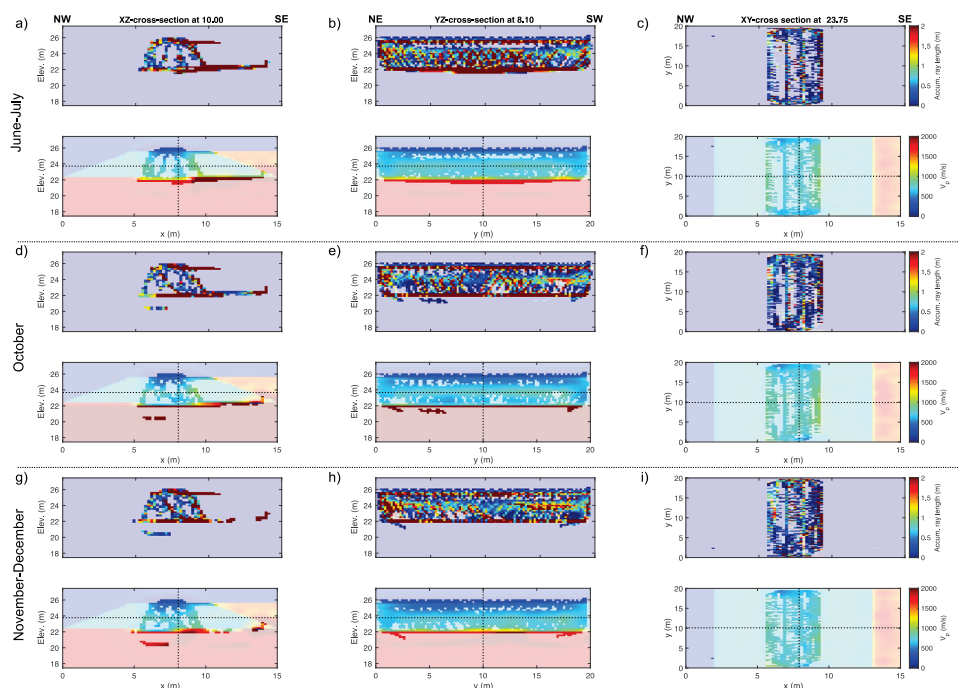
Energiforsk

Figure 41. Real P-wave traveltime tomography results, when shooting in the shallow/deep boreholes and in the water reservoir, for cross sections XZ, YZ and XY across and along the dam for recording campaigns in (a) (b) (c) June-July, (d) (e) (f) October, and (g) (h) (i) November-December 2020. From top to bottom the accumulated ray length per cell, and the inverted V_P model are shown in each cross section. Note that the solid colors indicate cells crossed by ray paths. The straight lines represented in the V_P model indicate the position along the x- and y-axis, and elevation of each cross section.

The inverted velocities are considerably lower than those expected for the materials in the dam. Apparent moveout velocities in the raw data for waves propagating through the filters are in the order of 1700-1800 m/s. Velocities in a saturated core are expected to be even higher. This discrepancy can be due to an overall delay in the instrumentation used or to the core not being fully saturated (most of the ray paths are through the core). An instrument delay would add an overall time delay to all picks. Picking on the peak, rather than the initial rise can also result in arrival times being too late. More analyses are necessary to investigate the discrepancy. However, relative velocities should be comparable so that the location of low velocity anomalies should not change with a constant shift in traveltime picks.

6 Data evaluation

6.1 POTENTIAL DEFECTS

Signs of diffractions have been identified in lines 1000, 4000, and 5000 when shooting in the shallow boreholes, and in lines 4000 and 5000 when shooting in the water reservoir. The diffractions may represent potential defects (diffractors). The traveltime of the apex of the diffractor represents the source-diffractor-receiver distance traveled by the ray. Assuming a constant velocity the diffractor position lies at any point along an elliptic path around a given source and receiver pair (see A in Figure 42). In the case where source and receiver lie in the same position, the ellipse collapses to a circle (B in Figure 42) and half of the calculated distance represents the distance from the receiver to the diffractor.
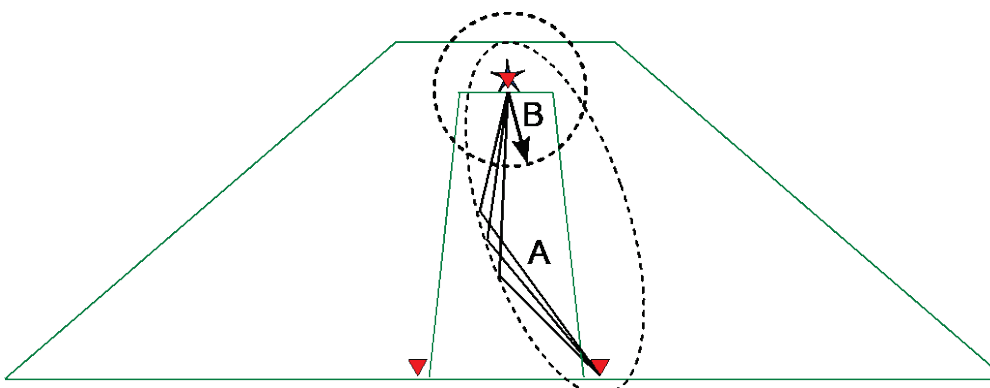

Figure 42, Schematic diffraction ray paths.

A total of five diffractors were evaluated as follows:

1. In Figure 14e, corresponding to the results from line 1000 collected in October 2020, we can recognize one diffraction, whose apex is located at CDP 122 (at about 8.8 m distance from the NE side of the profile, near the middle of the dam) and at around 1.7 ms. Using 1500 m/s velocity the distance to the apex is around 1.3 m. Assuming the defect to lie straight below the line its position is estimated at 8.8 m distance from NE corner and 2.2-2.3 m elevation from the base of the dam (considering that the shot and receivers were approximately located at 3.5-3.6 m elevation from the base of the dam).

2. Following the same procedure, in Figure 17cde, corresponding to the results from line 4000 collected in June-July, October and November-December 2020, a diffraction can be identified in all the sections more or less at the same position. The apex is located in CDP 127 (about 10.8 m distance from NE side of the profile) and at around 2.4 ms. Using 1500 m/s velocity, the source-diffractor-receiver distance is around 3.6 m, which is approximately the straight-line distance between the source and receiver. Knowing that the defects lie within the core, the position of the potential defect is estimated at 10.8 m distance from NE corner and above 1.8 m elevation from the base of the dam.

3. The results in line 5000 (Figure 18cd) for the recording campaigns in October and November-December 2020, show a diffraction whose apex seems to be located at different positions in both campaigns. Considering the data from November-December campaign, as the diffraction is clearer, the apex is located in CDP 129 (about 12 m distance from NE side of the profile) and at around 6.3 ms. Using 1500 m/s velocity, the source-diffractor-receiver distance is around 9.5 m. This places the diffractor below the concrete basement. However, more analysis and modeling are necessary to confirm this proposition. It is important that the correct velocities are used when determining the locations of the diffracting points.

4. In Figure 22bc, the results for line 4000, when shooting in the water reservoir, show a large diffraction, whose apex is located in CDP 168 (about 7 m distance from NE side of the profile) and at around 1.4 ms. Since the straight-line source-receiver distance is greater than 6 m a much faster velocity is needed to allow for a diffracted ray path. Assuming 4500 m/s velocity, the source-diffractor-receiver distance is around 6.3 m. This diffractor gets located below the concrete basement. An even higher velocity would produce a longer ray path, which would allow for a diffractor within the core. Again, more analysis and modeling are necessary to confirm this proposition.

5. The results in line 5000 when shooting in the water reservoir (Figure 23) show a large diffraction in all the recording campaigns. The diffraction apex is located in CDP 200 (about 10.2 m distance from NE side of the profile) and at around 1.9 ms. Using the same velocity of 4500 m/s, the source-diffractor-receiver distance is around 8.6 m. Again, this diffractor gets located below the concrete basement, but more modeling and analysis are needed.

6.2 SEISMIC MODELING

Ivandic and Juhlin (2018) performed seismic modeling prior to dam construction assuming the source and receivers were located on the dam crest. Given that the best quality data in the current project are acquired when the source is activated in the reservoir and data are recorded on the two hydrophone strings at the base of the dam (lines 4000 and 5000), additional modeling more representative of this geometry was done. The modeling was in 2D with the aim to better identify what corrections need to be made to the data in order to detect diffractions from potential defects. Figure 43 shows a plan view of the model looking down on the dam. Only three materials are considered in the modeling, water (pink), filters (blue) and the core (green). Two small defects were introduced into the core of the model, one at about 7 m along the dam close to line 4000 and one at about 13 m along the dam in the center of the core.

Figure 44 shows example synthetic data for all 100 sources recorded by two different receivers along line 4000. The diffraction from one defect is clearly visible on the receiver gather located 8 m from the left wall. Figure 45 shows the equivalent of Figure 44, but for line 5000. By applying standard processing methods to enhance the signal-to-noise ratio through stacking allows the diffraction apexes to be more clearly located (Figure 46 and Figure 47). The apexes indicate where along the line the diffractor is located. The timing gives an

indication of how far the diffractor is from the receiver. With 3D data it would be possible to located the diffractor in space. Note that for line 4000 (Figure 46) there is a difference in the timing of the apex locations of the diffractions, but for line 5000 the apexes of the two diffractions have the same timing. This is because the diffractions in line 4000 represent back scattering, while on line 5000 they represent forward scattering. There is no difference in the ray path length to the receiver (at the apex) for the two diffractors on line 5000, but the shape of the diffractions still differs.
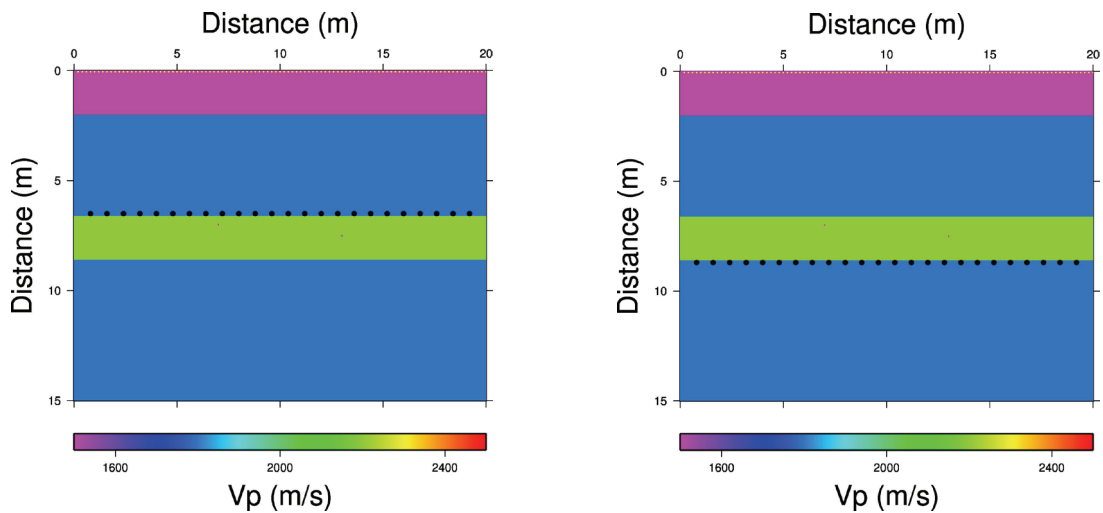

Figure 43. Simulated shooting geometry in the reservoir and recording on Line 4000 (left) and Line 5000 (right). There are two small diffractors (difficult to see) with a radius of 20 cm introduced in the core (green area). Pink color represents water and blue the filters. Black dots are the sensors. Source locations are the small red dots along the upper side of the model.
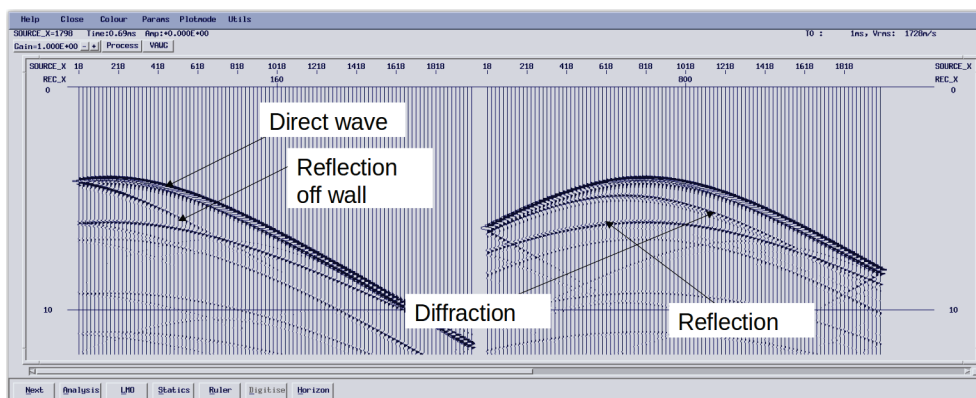

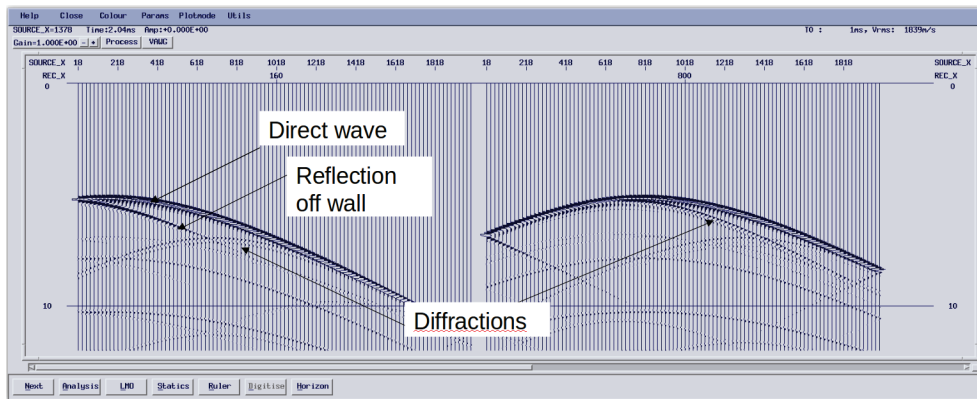**Figure 44. Example gathers for receivers at 1.6 and 8 m for line 4000.**

Figure 45. Example gathers for receivers at 1.6 and 8 m for line 5000.
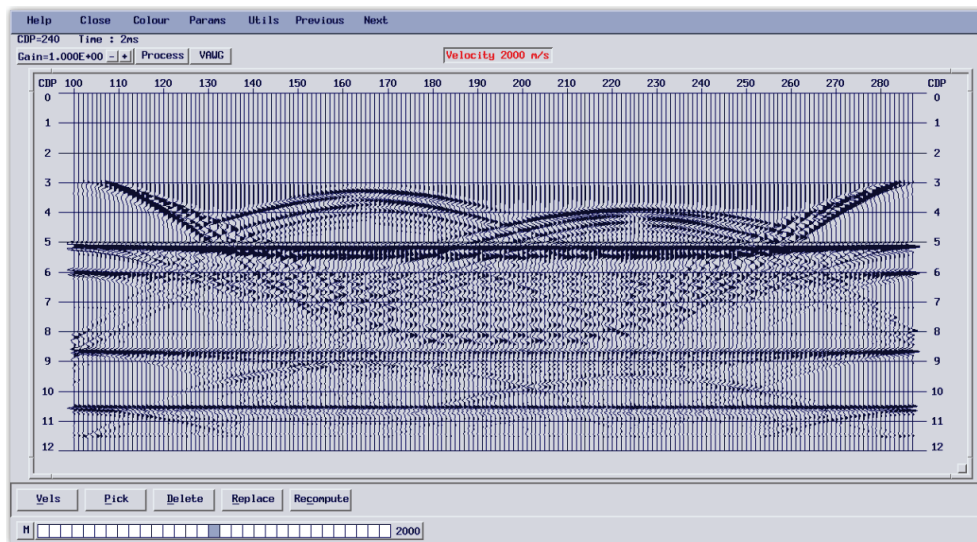

Figure 46. Diffractions stack coherently at a NMO velocity of 2000 m/s for line 4000.
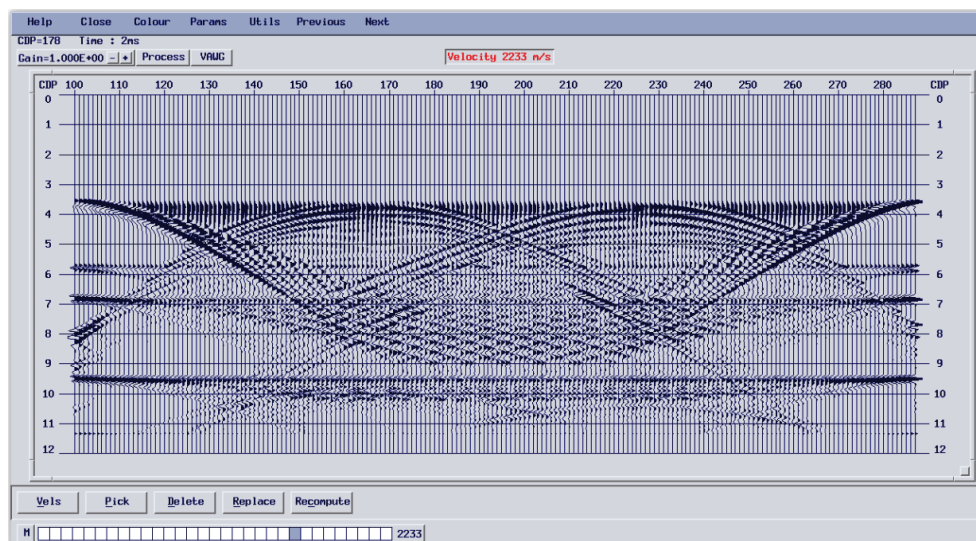
Figure 47. Diffractions stack coherently at a NMO velocity of 2233 m/s for line 5000.

6.3   LESSONS LEARNED

The frequency content registered in the hydrophone lines when shooting in the shallow boreholes (Figure 12) might be insufficient for detecting defects like the ones designed within the experimental dam in Älvkarleby (a minimum frequency of about 1500 Hz is required for detecting defects according to Ivandic and Juhlin 2018). The P-wave sparker SBS42 is able to produce very high-frequency seismic waves when shooting in the water reservoir, thus the seismic source behaves as expected in that position. However, when shooting in the shallow boreholes high-frequency seismic waves from the P-wave sparker source does not seem to propagate into the dam. Reflection seismic and P-wave traveltime tomography results may be affected by the lack of high frequency content. Two options could explain this behavior:

- The average activation depth of the seismic source is around 0.56 m, immediately above the core but not within it. The water level in the reservoir never reached higher than 3.3 m above the base of the dam, i.e. 0.24 m below the average source depth. Note also that the phreatic surface is probably even lower in the downstream direction. Therefore, the material surrounding the source outside the borehole is not saturated. This is the most likely reason for the lack of high frequencies.

- The manufacturer of the P-wave sparker SBS42 (Geotomographie 2021) indicates that the minimum operation depth should be no less than 1 m below water table. Although this requirement seems more related to safety issues, it is not clear if it could affect the behavior of the seismic source. This requirement was not fulfilled in the shallow boreholes on the crest of the dam, as the probe usually was submerged 0.4-0.5 m below water table. Testing of the source in the reservoir at the same depth would allow this hypothesis to be evaluated.

Installing the cable for shooting in the water reservoir successfully increased the frequency content of the seismic data. Additional measures, such as faster sampling rate of the recordings and decreasing the spacing between shot points (shooting 100 points), greatly improved the data and the possibility for detecting defects using the hydrophone lines.

Similarly, the use of a steel plug for covering the borehole when shooting with the P-wave sparker SBS42 in the dam proved useful in increasing the frequency content and may be worthwhile for future investigations in similar conditions.

If a similar experiment were to be performed again we would recommend having all receivers and sources in the saturated zone (when the dam is in equilibrium) for imaging potential defects. A recommended acquisition geometry would be to have all the sensors below the maximum water level of the reservoir on the upstream side. Sources could be placed in boreholes below the reservoir water level in the fine filter. Shooting in the reservoir itself should also be done, perhaps at different positions relative to the dam.

Estimates of V_S were provided only when shooting with the S-wave source BIS-SH. Picking S-wave arrivals was easier using this seismic source. Failure of the PVC casing in BH9000 was a drawback not only for obtaining more accurate estimates of V_S but also for not using the BIS-SH source in the following campaigns since it was clearly more powerful than the "CHE" crosshole energizer. It is not clear if the BIS-SH source was the cause of the casing failure. The failure could also be related to the difference in pressure generated by the pneumatic clamping system of the "CHE" crosshole energizer used in a previous campaign when the water reservoir was still empty.

Picking P- and S-wave arrivals requires high accuracy for obtaining accurate traveltime estimates and thereby seismic velocities. Manual picking, although accurate enough for a first approximation, could be improved with automated picking algorithms based on cross-correlation in order to reduce uncertainty and provide higher quality data. Further methods were investigated to improve this procedure, but the application of which was not feasible within this study.

Seismic velocities estimated from the crosshole measurements and from the tomography are lower than expected velocities for the dam materials. It is not clear why this is the case and more studies are necessary.

7 Conclusions

Possible defects are identified in several hydrophone lines when using the P-wave sparker SBS42 in the shallow boreholes located in the dam and in the water reservoir. However, there is some lack in consistency between the campaigns concerning the location diffraction apexes. Therefore no clear identification of defect locations have been made.

The frequency content is low when using the seismic source in the boreholes (1500 Hz is the minimum frequency for detection of the defects as indicated in a previous seismic modeling study by Ivandic and Juhlin, 2018); more studies are necessary for assessing all the data, e.g., seismic modeling, 3D seismic migration, and/or time-lapse processing.

Active seismic interferometry has potential for improving the seismic results in the uppermost meters. Passive seismic interferometry showed that velocity information on the dam could be extracted from the data. However, the virtual source gathers contain frequencies that are too low for seismic imaging. Noise levels were too high to be able to detect any flowing water within the dam.

Synthetic traveltime tomography results show, in general, the defect position, although P-wave velocity and size of the defects are not well recovered.

Real traveltime tomography results using data when shooting in the shallow/deep boreholes and in the water reservoir show velocities lower than expected for a saturated core, but perhaps realistic values if the core is partly saturated. The inverted V_P models seem to be better constrained when including data from the water reservoir. The tomographic models have velocity structure in agreement with the crosshole estimates. All the tomographic models in the YZ-cross sections indicate the presence of low velocity zones between 22 m and 24 m elevation, better defined in the inverted V_P model from Nov-Dec recording campaign (Figure 41). These zones could be related to potential defects.

The additional seismic modeling preformed using a simplified geometry with the sources in the reservoir and recording on the lowermost arrays provided insight into the expected location of diffractions in the source gathers and stacked sections. This modeling provides support for the interpretation of the diffractions in the stacked sections of the real data. Further future modeling may help determine if some of the observed diffractions are originating from with the dam or below the concrete foundation.

A large amount of data has been acquired (87 GB) and more analyses are needed to improve interpretation methods. Later ground truthing with the locations of the known defects may show characteristics in the data representing defects that have been overlooked.

8 References

Adamo N., Al-Ansari, Sissakian V. and Laue J. 2020. Geophysical methods and their applications in dam safety monitoring. Journal of Earth Sciences and Geotechnical Engineering, 11(1), 291–345. doi: 10.47260/jesge/1118

Cardarelli E., Cercato M. and De Donno G. 2014. Characterization of an earth-filled dam through the combined use of electrical resistivity tomography, P- and SH-wave seismic tomography and surface wave data. Journal of Applied Geophysics, 106, 87–95.

Deangeli C., Giani G.P., Chiaia B. and Fantilli A.P. 2009. Dam failures, Chapter 1. In: De Wrachien D. and Mambretti S. (Eds.) Dam-break Problems, Solutions and Case Studies, WIT Press, ISBN 978- 1-84564-142-9.

Geotomographie 2021. Information about borehole seismic sources and geophone available at: http://geotomographie.de/, last access: 2 March 2021.

Ikard S.J., Rittgers J., Revil A. and Mooney M.A. 2014. Geophysical investigation of seepage beneath an earthen dam. Groundwater. doi: 10.1111/gwat.12185

Ivandic M. and Juhlin C. 2018. Geophysical modelling for the Vattenfall experimental dam. Uppsala University, Dept. of Earth Sciences, report to Vattenfall.

Ivanov J., Miller R.D., Stimac N., Ballard R.F., Dunbar J.B. and Smullen S. 2006. Time-lapse seismic study of levees in southern New Mexico. SEG expanded abstract.

Ivanov J., Johnson C.D., Lane J.W. and Miller R.D. 2009. Near-surface evaluation of Ball Mountain Dam, Vermont, using multi-channel analysis of surface waves (MASW) and refraction tomography seismic data methods on land-streamer data. SEG expanded abstract.

Kargaranbafgui F. and Ghalamzan F. 2018. Application of seismic refraction and tomography methods to the assessment of the Sivaki dam site. International Journal of Engineering & Technology, 7(3), 1337–1345. doi: 10.14419/ijet.v7i3.12572

Kayode O.T., Odukoya A.M., Adagunodo T.A. and Adeniji A.A. 2018. Monitoring of seepages around dams using geophysical methods: a brief review. IOP Conference Series: Earth and Environmental Science, 173. doi: 10.1088/1755-1315/173/1/012026

Kim H.-S., Park H.G. and Yoo Y.S. 2006. Successive seismic reflection methods aided to find the change of structure and material properties in center core type earth-fill dam. In: Berga et al. (Eds.) Dams and Reservoirs, Societies and Environment in the 21st Century, Taylor and Francis Group, London, ISBN 0-415-40423-1.

Kim J.-H, Yi M.-J., Song Y., Seol S.J. and Kim K.S. 2007. Application of geophysical methods to the safety analysis of an earth dam. JEEG, 12(2), 221–235.

Matsuoka T., Onishi K., Shiraishi K. and Aizawa T. 2008. Site characterization by seismic interferometry method. In: Huang and Mayne (Eds.) Geotechnical and Geophysical Site Characterization, Taylor and Francis Group, London, ISBN 978-0-415-46935-4.

Miller R.D., Ivanov J., Hartung S. and Block L. 2004. Seismic investigation of a sinkhole on Clearwater dam. Symposium on the Application of Geophysics to Engineering and Environmental Problems. doi: 10.4133/1.2923253

Norstedt U. and Nilsson Aͦ. 1997. Internal erosion and ageing in some of the Swedish Earth and Rockfill dams, Q.73, R.20, 307 p. ICOLD Congress, Florence, Italy.

PASI 2021. Information about "CHE" CrossHole Energizer available at: https://www.pasisrl.it/, last access: 2 March 2021.

Powers M.H. and Burton B.L. 2008. Seismic refraction tomography in an urban environment using a vibrator source. Symposium on the Application of Geophysics to Engineering and Environmental Problems. doi: 10.4133/1.2963301

Sharma R.P. and Kumar A. 2013. Case histories of earthen dam failures. Seventh International Conference on Case Histories in Geotechnical Engineering, Chicago.

Tryggvason A., Rögnvaldsson S. ður T. and Flóvenz Ó.G. 2002. Three-dimensional imaging of the P- and S- wave velocity structure and earthquake locations beneath southwest Iceland. Geophysical Journal International, 151, 848– 866. doi:10.1046/j.1365-246X.2002.01812.x

Wapenaar K., Draganov D., Snieder R., Campman X. and Verdel A. 2010. Tutorial on seismic interferometry: Part 1 – Basic principles and applications. Geophysics, 75(5), 75A195–75A209. doi: 10.1190/1.3457445

Woolery E.W. 2018. SH-mode seismic reflection imaging of earthfill dams. Engineering, 4, 694–701.

Energiforsk

SEISMIC INVESTIGATIONS AT THE VATTENFALL EXPERIMENTAL DAM, ÄLVKARLEBY, SWEDEN

In this project, a seismic method is evaluated at the Vattenfall experimental dam. The dam was equipped with seismic cables and hydrophones and trials were conducted during six measuring campaigns.

This report summarizes the findings from these experiments and also gives suggestions on how to build upon the achieved results and how to develop the method further.

LULEÅ TEKNISKA UNIVERSITET

Energiforsk